JOINT EUROPEAN TORUS

JET–P(92)96

G.A. Cottrell, V.P. Bhatnagar, O. da Costa, R.O. Dendy, J Jacquinot,
D.C. McCune, M.F.F. Nave, P. Smeulders, D.F.H Start.
and JET Team

Ion Cyclotron Emission Measurements during JET Deuterium-Tritium Experiments

Ion Cyclotron Emission Measurements during JET Deuterium-Tritium Experiments

G.A. Cottrell, V.P. Bhatnagar, O. da Costa, R.O. Dendy[1], J Jacquinot, D.C. McCune[2], M.F.F. Nave[3], P. Smeulders, D.F.H Start. and JET Team*

JET-Joint Undertaking, Culham Science Centre, OX14 3DB, Abingdon, UK

[1] AEA Fusion, Culham Laboratory, Abingdon, Oxon, OX14 3DB
[2]Princeton Plasma Physics Laboratory, Princeton University, Princeton, NJ, USA
[3]Associacao EURATOM/1ST, Lisbon and LNETI, Sacavem, Portugal
** See Annex*

Preprint of Paper to be submitted for publication in Nuclear Fusion

ABSTRACT.

In the course of the Preliminary Tritium Experiment in JET, where combined deuterium and tritium neutral beam injection generated a DT fusion power of 1.7MW, ion cyclotron emission (ICE) was measured in the frequency range $\nu \leq 180$ MHz. The ICE spectra contain superthermal, narrow, equally spaced emission lines which correspond to successive cyclotron harmonics of deuterons or α-particles at the outer mid-plane, close to the last closed flux surface at major radius R ~ 4.0m. The ICE signal fluctuates rapidly in time, and is extinguished whenever a large-amplitude edge-localized mode (ELM) occurs. Power spectra in DD and discharges are similar in form, but on changing from pure D to mixed D + T neutral beam injection, the intensity of the ICE rises in proportion to the increased neutron flux. This indicates that fusion a.-particles - and not beam ions - provide the free energy for generating ICE. The JET ICE database, which now extends over a range of six decades in signal intensity, shows that the time-averaged ICE power increases almost linearly with total neutron flux. The rise and fall of the neutron flux during a single discharge is closely followed by that of the ICE, which is delayed by a time of the order of the fusion product slowing-down time. This feature is well-modelled by TRANSP code simulation of the density of deeply trapped fusion products reaching the plasma edge. Calculations reveal a class of fusion products, born in the core, which make orbital excursions of sufficient size to reach the outer mid-plane edge. There, the velocity distribution is both anisotropic and not monotonically decreasing, and is potentially unstable to relaxation at multiple ion cyclotron harmonics. The results are discussed in the context of collective emission models in which cyclotron harmonic radiation is excited by a diffuse, high energy ion population. This paper shows how ion cyclotron emission provides a unique diagnostic for fusion a.-particles.

1. INTRODUCTION

The original motivation for measuring ion cyclotron emission (ICE) from a large, hot, dense tokamak plasma, such as that produced in JET [1] (major radius R = 2.96 m, minor radius a = 1.2 m), arose from the possibility of observing optically thick harmonic emission from the thermal ions. However, in JET deuterium plasmas, it has been found that the confined superthermal population of charged fusion products radiates strongly at ion cyclotron frequencies [2]. Thus ICE observations offer a possible method for measuring the characteristics of energetic charged particles in magnetic fusion experiments. We recall that in pure deuterium plasmas, the following primary fusion reactions take place with equal probability:

$$D + D \rightarrow {}^3He(0.82MeV) + n(2.5MeV), \tag{1}$$

$$D + D \rightarrow T(1.0MeV) + p(3.0MeV). \tag{2}$$

In addition, secondary reactions can take place between the energetic products of fusion reactions (1) and (2) and the deuterons:

$${}^3He + D \rightarrow p(14.6MeV) + {}^4He(3.7MeV) \tag{3}$$

$$T + D \rightarrow {}^4He(3.6MeV) + n(14.0MeV). \tag{4}$$

For deuterium-tritium plasmas in the ion temperature regimes of present tokamak experiments ($T_i \sim$ 10 keV - 20 keV), fusion reaction (4) is dominant by virtue of the relatively large ratio of DT to DD cross-sections.

ICE has previously been observed in a number of pure deuterium-fuelled tokamaks at frequencies $\nu \leq 500$ MHz, and we begin by reviewing the data obtained. On TFR tokamak [3], superthermal ICE from the peripheral region of the plasma was found. A similar result [4] was found on JET tokamak where the ICE spectra showed narrow ($\Delta\nu/\nu \sim 0.1 << a/R \sim 0.4$) superthermal emission lines, superimposed on a broad background continuum, with regular spacing proportional to the magnetic field. These observations confirm the cyclotronic character of the emission, and further indicate that the detected ICE originates from a localised region of radial extent $\Delta R \cong 20$ cm. In JET ohmically heated deuterium discharges [2], the intensity of the ICE lines increased linearly with the DD fusion reaction rate over three orders of magnitude in signal intensity, indicating that charged fusion products provide the free energy to drive ICE. By applying frequency-matching considerations to JET ICE data

[5], it was shown that the frequencies of the emission lines coincide uniquely with harmonics, l, of the deuteron (degenerate with the α-particle) gyrofrequency, evaluated in the total field at the position of the outer mid-plane edge: $\omega = l\ \Omega_D = l\ \Omega_\alpha$, where Ω_D and Ω_α are, respectively, the gyrofrequencies of the bulk deuterons and α-particles. The signals apparently originated in the the near-field region of the detecting ICRH antenna on JET. In addition, time-resolved ICE signals on JET high current ohmically heated discharges correlated with inverted sawteeth [6], seen in data from edge soft X-ray and D_α diagnostics.

ICE measurements have also been made on TFTR tokamak using RF probes mounted *above* the plasma [7]. With deuterium neutral beam injection (NBI), the spectra showed cyclotron harmonic peaks with frequencies corresponding to the edge $\omega = l\ \Omega_D = l\ \Omega_\alpha$, a result in qualitative agreement with the JET results. However, in ohmically heated discharges, a different set of lines was seen with frequencies related to the *odd* deuteron harmonics: $\omega = (l + 1/2)\ \Omega_H$. Thus lines with frequencies $\omega = l\ \Omega_D$ (l = 2, 4, 6, ...), seen in JET ohmic data, were apparently missing from the TFTR data. Although this difference is not understood, both sets of data point to localization of the cyclotron harmonic emission at the outer mid-plane edge of the tokamak. At higher frequencies (~ 100 MHz ≤ ν ≤ ~ 350 MHz), a broadband feature was found in the TFTR data, peaking at a frequency of ν ~ 150 MHz. The intensity of this feature was found to follow the time evolution of the neutron emission. More recent observations [8] with deuterium NBI on TFTR show emission lines which correspond to the edge ion cyclotron harmonics of ^3He ions, in addition to those of the deuterons. Such ions could be produced by fusion reaction (1) above.

In summary, there is strong experimental evidence that a minority fusion product population in a deuterium plasma can excite superthermal ICE with spectral peaks at multiple cyclotron harmonics in the outer mid-plane edge of a tokamak plasma. The aim of the present series of measurements on JET was to acquire new data to provide a better understanding of the ICE mechanism which, in turn, is important in assessing the potential of ICE as a diagnostic for confined energetic fusion α-particles in DT plasmas. The JET Preliminary Tritium Experiment (PTE) [9] therefore offered an ideal opportunity to monitor ICE from a large tokamak plasma in which the fusion product population was dominated by energetic α-particles, produced by DT reaction (4), and not by the products of DD fusion reactions. Some preliminary data on the PTE ICE experiment have already been reported [10]. However, in this paper, a more detailed analysis of the experimental data and discussion of possible models is presented. A description of the experimental method appears in section 2, together with an assessment of the experimental uncertainties. Section 3 contains the results of the ICE measurements: these include power spectra for DD and DT NBI-heated discharges, the relationship between the ICE power detected and the α-particle content of the plasma calculated using the TRANSP [11] Monte-Carlo model, and a comparison of the time-evolution of ICE with the α-particle content of the DT plasma. The correlation between

ICE signals and MHD events - sawteeth and edge localized modes (ELMs) - is also described. Section 4 summarises the general properties and status of the ICE data and the challenge that these present to theoretical models of the emission mechanism. Calculations of the structure of the energetic ion distribution are presented in Section 5, showing the existence of a class of trapped particles which are born close to the centre but intercept the outer edge plasma, contributing to a velocity distribution which is anisotropic, radially inhomogeneous and not monotonically decreasing. We discuss the degree to which the threshold for a thermonuclear velocity space instability is exceeded in JET DT discharges. Finally, Section 6 contains a discussion of the results.

2. EXPERIMENTAL METHOD

In the PTE series of NBI-heated hot-ion H-mode discharges [9], the plasma was configured as a single-null X-point discharge, with reversed toroidal field so that the ion ∇B drift was directed away from the upper dump plates. The PTE series contained discharges in which both deuterium NBI and combined deuterium and tritium NBI was used. The measured plasma parameters of the highest performance DT discharge are shown in Table I, together with some selected parameters derived from TRANSP code simulation[1]. In the DT cases, two discharges (Pulse Nos. 26147 and 26148) were made with 100 % tritium feed to two neutral beam injectors with 78 keV acceleration, delivering 1.5 MW out of a total of 14.3 MW. In addition, a number of discharges were made with an admixture of 1 % tritium in deuterium fed to two neutral beam injectors. In general, it was possible to distinguish two separate phases of each discharge: first, a good confinement H-mode phase associated with rising total neutron flux and large stored energy content [12] and, second, a subsequent termination phase [13] in which the total neutron flux declined, as did the stored energy. The transition between these two phases was characterized by one of the following: an 'X-event', defined as the time at which the total bolometric radiated power showed a spike of order 10 MW - 30 MW, with simultaneous increase of the X-point target temperature of the order of 100° C; a 'bloom', defined as the roll-over of the deuterium density due to impurity dilution; or loss of confinement, defined as the roll-over of the total stored energy of the discharge. ICE measurements were made throughout the PTE series of discharges.

[1]In the TRANSP simulation results quoted in this paper, the radial profile of the average effective ionic charge of the plasma, Z_{eff}, was taken from active Charge Exchange Recombination Spectroscopy measurements. In the TRANSP simulation quoted in Ref. [9] the Z_{eff} profile was assumed to be flat, with a fixed value given by visible bremssstrahlung measurements. The present procedure results in a minor difference in the estimated central thermal ion density quoted in Table I.

To monitor the ICE, a two-element fast wave ICRH antenna was used in reception mode as a probe (Fig.1). The two elements of the antenna could be phased to produce either a monopole or a toroidal dipole $k_{\|}$ wavenumber spectrum (parallel to the magnetic field). In the monopole configuration, the antenna spectrum was centred on $k_{\|} = 0$, with a spread of $k_{\|} = \pm$ 4 m^{-1}, and in the dipole configuration, the reception pattern peaked at $k_{\|} = \pm 7$ m^{-1}, with a null at $k_{\|} = 0$. Each antenna element was connected directly to the measurement system via two transmission lines (length $L \sim 80$ m, impedance $Z_0 = 30\ \Omega$) which have negligible loss. The power coupled to a matched load is given by

$$P_{ICE} = P_{plasma}\,(1-|\rho_c|^2), \tag{5}$$

where P_{plasma} is the radio frequency power incident on the antenna surface, the voltage reflection coefficient is

$$\rho_c = \frac{Z_0 - R_c}{Z_0 + R_c}, \tag{6}$$

and the coupling resistance of the antenna is R_c. For the JET antenna system, $Z_0 >> R_c$, and $P_{ICE} \cong (4\ R_c\ /\ Z_0)\ P_{plasma}$, showing the detected RF power to be proportional to R_c. Typical values of R_c are ~ 5 Ω and ~ 2.5 Ω for the monopole and dipole cases respectively. At the termination of the transmission lines, two transformers - one for each line - were used to match the line impedance to the 50 Ω analyser impedance. After combining the incoming signals with appropriate phase, the RF signal was split equally to two spectrum analysers. These were used to monitor the ICE spectrum in a range typically $0 \le \nu \le 100$ MHz or $0 \le \nu \le 200$ MHz by cyclically sweeping the analyser (SA1), and to monitor the time behaviour of the ICE at fixed frequency (SA2). In the SA1 path, the incoming signal was mixed with calibration lines at 25 MHz and 50 MHz to provide a reference which was stored with the data. This procedure enabled data from different discharges to be cross-compared with minimal error. The bandwidth of each analyser was 1 MHz in these experiments. For $\nu > 180$ MHz, the impedance-matching transformers introduced a severe attenuation in the frequency response, effectively defining an upper limit of $\nu = 180$ MHz on the bandpass. Spectra presented here have been corrected for the measured transformer response below this frequency, and have been truncated above it where the correction was so large as to be untrustworthy. No correction has been applied for the frequency response of the antenna-plasma coupling. Small impedance mismatches at the terminations of the transmission lines led to the transfer function of the system being modulated by a pattern of modes with spacing $\Delta\nu_{mode} \cong c_L\ /\ 2L \sim 1.8$ MHz, where c_L is the velocity of light in the transmission line. In the

spectra presented below, this structure was removed by smoothing the data with a 1.8 MHz filter, in effect limiting the resolution of the ICE measurements.

3. EXPERIMENTAL RESULTS

3.1 The Power Spectrum

Two ICE spectra are shown in Fig. 2, each taken just before the peak of the neutron emission in similar PTE discharges. Pulse No. 26140 was run with pure deuterium NBI and pulse No. 26148 with mixed deuterium and tritium NBI. Although differing in relative signal intensity, both spectra are similar in form, showing up to seven clearly identifiable and regularly spaced emission lines with narrow relative widths $\Delta\nu / \nu \approx 0.09 << a / R = 0.38$. In both cases, the spacing of the line centres is 17 MHz ± 0.5 MHz. A plot of the deuterium cyclotron frequency $f_{cD}(R)$ (calculated in the total magnetic field) against major radius, R, is shown in Fig. 3. The plot shows that the spacing of the ICE line centres correctly matches the cyclotron frequency of deuterons or α-particles at a unique value of the major radius, $R = 4.0$ m ± 0.1 m. The radius of the Faraday screen of the ICRH antenna was at $R_{ant} = 4.15$ m, thus the emission is localized to a region close to the JET antenna. For the lower harmonics ($l \leq 7$) in the spectra of Fig. 2, the even-l lines are more intense, by up to a factor of 10. However, this feature does not appear to be a general rule, since inspection of other discharges reveals a greater degree of variability in the relative amplitudes of the sequence of lines.

A comparison between ICE spectra obtained using both the dipole and monopole antenna phasing is shown in Fig. 4, for two similar discharges with 1 % tritium NBI, (monopole case: pulse No. 26095; dipole case: pulse No. 26108). To reduce the effect of data variability, and to help reveal any clear systematic changes in the spectra, two successive spectral sweeps in each discharge were averaged together during the period of significant neutron emission. For the dipole, the lower-l lines tend to be of lower amplitude, by between 5 dB - 10 dB, compared with the monopole case. The $l = 6$ lines are, however, comparable in amplitude. Earlier work [2] has shown that the intensity of an ICE line increases linearly with the total neutron flux. Part of the amplitude difference seen in Fig. 4 can be accounted for by the fact that the total neutron flux was a factor of 2.2 larger in the discharge with the monopole phase. To reveal any underlying systematic differences in the ICE power detected between the two cases, the spectra of a number of similar discharges were averaged in a frequency range 10 MHz $\leq \nu \leq$ 80 MHz, containing the first four bright harmonic lines. It was found that the monopole dataset contained, on average, spectra more intense by a factor ~ 2 than those in the dipole dataset. This factor is consistent with the expected factor of increase in the antenna coupling resistance (and therefore in ICE power coupled to the

spectrum analyser given by Eq.(5)) on changing from dipole to monopole configuration. We conclude therefore that, once allowance is made for the coupling resistance of the antenna, there is no significant evidence that the total ICE power that is detected is sensitive to the phasing of the JET antenna. This result shows that the power spectrum contains components with wavevectors in the acceptance range of the antenna: $0 \leq | k_{\parallel} | < \sim 7\ m^{-1}$.

Spectral lines from both DD and DT discharges show evidence of fine structure, which can be seen in Figs. 2 and 4. With increasing harmonic number, the lines appear to split into blended doublet or triplet shapes, with a linewidth given approximately by the relation $\Delta\nu / \nu \sim 0.06$. For the higher harmonics, the full-width of the split lines becomes comparable with the inter-harmonic spacing (17 MHz). Above a frequency $\nu \sim 100$ MHz, the lines blend together into an intense continuum feature. The total power in the spectrum, integrated over the frequency range displayed in Fig. 2 is, in fact, dominated by the continuum component. The sum of the individual emission powers of the first seven clearly visible ICE harmonics represents a fraction of only ~ 2 % of the total integrated emission power in the spectrum.

3.2 Correlation Between the ICE Intensity and the Neutron Flux

In plasmas with intense NBI heating, the issue of whether beam particles or fusion products drive the ICE was resolved by comparing the level of ICE power between two similar PTE discharges with pure D → D NBI (as a control experiment), and with mixed D + T → D NBI. This comparison was made at the time of peak neutron emission (Table II). The results show that, by changing from pure D to mixed D + T NBI at almost constant P_{NBI}, the ICE power increased by a factor comparable with the total neutron flux, whilst in both cases the content of beam particles in the plasma was almost constant. This shows clearly that the ICE is not driven by beam particles. In the DT case, the fusion product population of the plasma was generated predominantly by DT - and not DD - fusion reactions, showing clearly that the fusion α-particles are responsible for the increased intensity of ICE. We may add that no new lines corresponding to triton cyclotron harmonics were observed in discharges with tritium injection.

For a wide variety of JET discharges, with ohmic heating in deuterium, with pure D → D NBI, and with mixed D + T → D NBI, the detected ICE power has been plotted as a function of the total neutron flux R_{NT} in Fig. 5. The groups of data shown have been drawn from a database of JET ICE experiments performed between 1985 and 1991. Each data point marks the level of the ICE emission at the peak of the $l = 2$ line, which was chosen because its frequency typically lies near the resonant frequency of the ICRH antenna, $\nu \cong 33$ MHz. Uncertainties in the relative calibration between data groups arise mainly from inter-shot differences in the antenna coupling resistance; these are estimated to result in uncertainties of ± 6 dB in detected RF power. Fig. 5 shows that the measured level of the ICE power is

almost proportional to the neutron flux over a range of six orders of magnitude; the best fitting relation is $P_{ICE} \propto R_{NT}^{0.9}$. The error in the exponent is ± 0.1, thus these data are consistent with a linear relationship. The total ICE power radiated into 4π steradians at the time of the peak neutron emission in pulse No. 26148 would be of the order of a few watts, assuming poloidal uniformity and that the coupling efficiency of the antenna is constant in the measured frequency range. This radiative power loss is a small fraction ~ 10^{-5} of the total α-particle heating power $P_\alpha \cong 235$ kW deduced from TRANSP [11] code simulation (Table I) using a Monte-Carlo model to describe the evolution of the α-particle population.

3.3 Correlation Between ICE Intensity and the α-Particle Density

The TRANSP plasma simulation code was used both to check the internal consistency of the measured diagnostic data and to compute the spatial and temporal evolution of the energetic fusion α-particles. The Fokker-Planck equation describing the slowing-down of the fusion products was solved using a Monte-Carlo technique. This method was employed so that an accurate assessment of the finite orbit effects for the fast ions could be obtained. In this model, the fast ion guiding-centre trajectories, the thermalization α-particle source, and the collisional heating rate of the background plasma are computed. The fusion ion source was assumed to be isotropic and monoenergetic in the reference frame of the plasma. Although this is a good assumption in the case of α-particles produced by thermal-thermal DT reactions, it does not represent the birth distribution for the α-particles produced by beam-thermal DT reactions with full accuracy. Applying kinematic considerations to the two-body T → D reaction shows that the fusion α-particles produced in NBI beam-thermal collisions, are born with a spread of energies in the laboratory frame. This ranges from E_α = 3.5 MeV - 0.7 MeV = 2.8 MeV (in the direction opposite to the motion of the beam ion) to E_α = 3.5 MeV + 0.8 MeV = 4.3 MeV (in the forward direction with respect to the motion of the beam ion) for the tritium beam injection energy of 78 keV used in the experiments. Approximately half the α-particles were produced by beam-thermal DT reactions in the two pulses Nos. 26147 and 26148. We therefore expect some angular and energy spread in the birth distribution of the α-particles in the experiments. Fast ion radial density profiles were computed as flux-surface averages, and the α-particle profile for DT pulse No. 26148 is shown in Fig. 6. The effect of including the finite Larmor radii of the fast ions is to broaden the density profile, an effect which is particularly significant in the edge region. This effect was estimated by convolving the TRANSP α-particle radial density profile with the α-particle Larmor radius, and is shown in Fig. 6. For trapped energetic fast ions, the orbit geometry gives rise to strong poloidal asymmetry, favouring population of the low-field side of the torus. Thus the flux-surface averaged fusion product density shown in Fig. 6 underestimates the true local number density at the outer edge of the plasma. For trapped orbits of the type

shown in Fig. 14(b), the local density of fusion products at the outer mid-plane edge, $R = 4.0$ m, is approximately six times larger than the value calculated by flux-surface averaging. Allowing for the effects of finite α-particle Larmor radius and of poloidal asymmetry, we estimate that, at the location of the ICE source and given the conditions of Fig. 6, the local density of energetic α-particles is $n_\alpha(R = 4.0\ \text{m}) \sim 10^{15}\ \text{m}^{-3}$. This is considerably smaller than the central value, $n_\alpha(R = 3.13\ \text{m}) \approx 2.6 \times 10^{16}\ \text{m}^{-3}$.

Traces from the fixed-frequency spectrum analyser show large (~ 100 %) fluctuations in the ICE amplitude at the data sampling frequency (2 kHz). The bursts are therefore coherent within the emission volume: if this were not the case, and the emission volume contained multiple randomly bursting emission regions, the resulting depth of modulation would be less than 100 %. In order to compare the fluctuating ICE signal with the calculated densities of α-particles, individual spectra were therefore averaged in the available range of the swept analyser, 10 MHz -180 MHz, to yield a signal representing the average ICE power in that bandwidth. A comparison of the temporal evolution of the integrated ICE signal with the measured total 14.7 MeV neutron flux is shown in Fig. 7. Up to the time of the X-event (t = 13.28 sec), the integrated ICE signal followed the neutron emission, but was delayed by a time ~ 0.5 sec. We found a delay of similar magnitude in D → D NBI discharges, and the effect has also been observed in D → D NBI discharges on TFTR [7]. The delay of the ICE signal with respect to the rise of the neutron flux is comparable with the time needed to build up a population of fusion products, namely the fusion ion-electron slowing-down time τ_s. During the rise phase of the 14 MeV neutron emission between 12 sec and 13.28 sec in DT pulse No. 26148 (Fig. 7), the volume-averaged value of τ_s is in the range 0.6 sec - 0.7 sec, a value consistent with the observed delay. A comparison of the temporal evolution of the integrated ICE signal with the total number of energetic α-particles N_α - as given by the Monte-Carlo calculations - is shown in Fig. 7. The ICE data point with the largest signal intensity has been normalized to the peak number of α-particles for comparison. Up to the time of the X-event, the ICE signal correlates reasonably well with the calculated total number of α-particles. However, between 12.5 sec and 13.3 sec, the ICE increases more rapidly than N_α.

As noted above, frequency matching considerations for the harmonic ICE spectral peaks imply a major radius of $R = 4.0\ \text{m} \pm 0.1\ \text{m}$ for the location of the source of emission. It is therefore appropriate to compare the ICE signal with the evolution of the number density of α-particles at the plasma edge. As we shall discuss in Section 4.2, the fusion product population in the outer edge plasma is dominated by particles which are born in the core, but whose drift orbits undergo large radial excursions. Fig. 8 shows a comparison of the time-evolution of the ICE data and of the number density of α-particles at three major radii from the centre to the edge of the plasma: $R = 3.13$ m, 3.38 m, and 4.02 m. The peak of each curve has been normalized to the largest ICE data point. The sudden drops in the two innermost α-

particle density traces are the result of the sawtooth model used in the TRANSP simulation. In this, the sawtooth is assumed to redistribute all the fast ions inside the $q = 1$ surface (normalized radius $r/a \sim 0.36$) uniformly in a mixing region of normalized radius $r/a \sim 0.51$. Up to the time of the first sawtooth, the ICE data lie significantly below the two innermost α-particle density traces. At the time of the sawteeth, there is clearly no significant response in the ICE signal, a feature shared by the edge α-particle density trace. Up to the time of the X-event, however, the ICE data and the edge α-particle density trace are closely correlated. The best fit between the measured ICE data points and the evolving α-particle density curves occurs for major radii between $R = 3.93$ m and $R = 4.02$ m, a feature consistent with the results of frequency matching to the ICE spectral lines (Fig. 2).

After the time of the X-event, during the termination phase, the discharge showed a period of intense edge MHD activity with the appearance of large-amplitude ELMs. This phase also coincided with observations of enhanced, broadband fluctuations in edge density revealed by the microwave reflectometer diagnostic. As discussed below, in Section 3.3.2, this activity strongly affected the ICE measurements. Thus, after the X-event time ($t = 13.28$ sec) in this discharge, it should be noted that the spectrally-integrated ICE data shown in Figs. 7 and 8 were distorted by these effects.

3.3 Correlation of the ICE with MHD Observations

3.3.1 Central MHD Activity ($m = 1$, $n = 1$)

Earlier ICE observations in JET high current ($I_p = 6$ MA) ohmically heated discharges [5] show clear evidence of positive correlation between ICE fluctuations and sawtooth collapses. The ICE signal increases ~ 20 ms after the central sawtooth collapse, a delay comparable with the measured propagation time of the heat pulse to the edge. Fig. 9 shows the time variation of the fixed frequency ($\nu = 33$ MHz) ICE signal during the good confinement phase of DT pulse No. 26147. The times of three sawtooth collapses are marked. Following each sawtooth collapse, there is a small fluctuation in the ICE signal. Inspection of other discharges in the PTE series revealed some further correlations with inverted sawteeth, although in these lower current ($I_p = 3.1$ MA) discharges the correlation is not as clear as that observed in the higher current discharges. In some cases, sawtooth collapse produces no observable change in the ICE signal. In addition, we have found no convincing evidence for correlation of the ICE fluctuations with fishbone bursts. Therefore, in the PTE discharges, there is no consistent evidence for correlation between ICE fluctuations and central $m = 1$, $n = 1$ activity.

3.3.2 Edge-Localized MHD Modes (ELMs)

A variety of ELM phenomena has been observed in JET H-mode discharges. For comparison with the ICE signal, we divide the ELMs into two classes: large and small amplitude ELMs. The small ELMs perturb only the outermost few centimetres of plasma, whereas the large ELMs penetrate to depths of between 10 cm and 30 cm. Radically different behaviour in the ICE signal is observed in the two cases.

Small amplitude ELMs are commonly observed, for example, in the L to H transition and during the early part of the good confinement phase of the high performance PTE discharges. Examples of these are shown by the D_α spikes in Fig. 9. Time-resolved data show a number of discrete ICE amplitude fluctuations of approximate duration 20 ms, and amplitude ΔP_{ICE} / $P_{ICE} \sim 1$ which, in general, correlate positively with these ELMs. As noted in Section 2, the detected ICE signal is proportional to the product of the ICE source power in the plasma with the antenna-plasma coupling resistance R_c , which is always observed to increase when ELMs occur. During ICRH heating experiments in the presence of ELMs, fluctuations of magnitude ΔR_c / $R_c \sim 1$ are commonly observed. Thus, during the good confinement phase of the discharge, the positive correlation observed between ICE and small amplitude ELMs is consistent with ELM-induced changes in R_c, and not with any change in the intrinsic strength of the ICE source. Corresponding soft X-ray data reveal only small amplitude perturbations in the outermost few centimetres of the plasma. We infer that these small amplitude ELMs do not penetrate sufficiently far into the edge plasma to disturb the ICE source.

During the termination phase of PTE discharges, ELMs of significantly larger amplitude are observed. Examples of large amplitude ELMs coinciding with the X-events in DT discharges are shown in Figs. 9 and 10. Coincident with the appearance of a large ELM, the ICE signal vanishes in a time < 500 μs. We conclude from this that the large amplitude ELM is associated with the prompt loss of α-particles from the edge. In both DD and DT discharges, the ICE vanishes at the time of each large amplitude ELM. An example of this behaviour is shown in Fig. 10 for DT pulse No. 26148, in which a sequence of large amplitude ELMs, having repetition times in the range of 60 ms - 100 ms, was observed after the X-event. For this discharge, the fixed-frequency spectrum analyser was tuned to 165 MHz, close to the $l = 10$ harmonic of the edge α-particle cyclotron frequency. Inspection of the corresponding ICE spectra revealed that lines with harmonic numbers $l = 3$ - 9 were completely absent for a period approximately 20 ms following each ELM. No coincidence data was available for the $l = 1$ and 2 harmonic lines in this discharge. Simultaneous soft X-ray data show large perturbations penetrating to a depth of between 10 cm and 30 cm in the edge plasma, which encompasses the ICE source. We infer that the large amplitude ELMs terminate the ICE by expelling fast ions, thereby temporarily extinguishing the source. This behaviour is consistent with the localization of the ICE source in the edge, and shows also

that there is little or no contribution to the ICE signal from the fusion products that are confined to the discharge core. Fig. 10 also shows the behaviour of the line-integrated electron density in an outer channel of the millimetre-wave multi-channel interferometer, having line-of-sight tangent to the magnetic flux surfaces at major radius R = 3.75 m. At the time of the X-event, there is a sudden upward step in the edge density. Subsequently, the trace shows transient increases correlated with the ELMs. The Abel-inverted density profile shows that this density step is particularly significant for major radii between $R \sim 3.7$ m and the outer edge, and persists for the ELM phase shown in Fig. 10. An increase in the plasma density in front of the ICRF antenna increases the antenna-plasma coupling resistance, leads to a corresponding increase in the ICE power detected. This effect may explain the increase in the peak level of detected ICE intensity seen after the time of the X-event in Fig. 10.

The time-expanded traces of Fig. 11 show that each successive ELM in the sequence annihilates the ICE for a period of ~ 20 ms before a new phase of growth occurs. During this temporary period of ICE-quiescence, microwave reflectometer data show a high level of broadband edge plasma density fluctuations with frequencies up to 100 kHz [14]. These fluctuations coincide with the period when the D_α signal remains above the background level. As the D_α signal decays, a new phase of ICE growth commences, consisting initially of slow growth for a time of ~ 15 ms, followed by rapid growth. During the phase of rapid growth, magnetic coil data show bursts of 4.5 kHz MHD oscillations. The form of the growth of these oscillations is initially exponential, but subsequently follows a linear law; this latter phase coincides with a saturation of the ICE signal. Eventually the ICE and MHD oscillations are both terminated by the next ELM. Soft X-ray data (Fig. 11) show a deformation associated with the mode which is largest at the q = 2 surface (which intersects the outer major radius at $R \sim 3.8$ m), indicating an m = 2, n = 1 mode. The 4.5 kHz MHD mode has not been observed in any of the 1 % tritium PTE discharges or in other similar DD discharges, and it appears to be a unique observation in the two 100 % tritium PTE discharges.

X-events can also occur without the prompt disappearance of the ICE signal, as shown in Fig. 12. In pulse No. 26095, the X-event occurs at t = 13.78 sec. Tomographic reconstruction of the soft X-ray emission prior to the X-event shows a peaked profile, characteristic of a phase of good confinement. However, at t = 13.78 sec, the total neutron flux starts to fall and there is a modest drop in central β coincident with a radiation spike of amplitude $P_{rad} \sim 15$ MW. The ICE signal showed a transient increase lasting ~ 20 ms, but, unlike the case of pulse No. 26148, survived the X-event. At this time, the soft X-ray emission contours show a relatively slow flattening of the profile, and there is only a mild deformation in the edge region at $R > 3.7$ m, a feature which can also be seen in Fig. 13. However, at time t = 14.13 sec, a faster event occurs, which affects a large region of the profile causing a significant drop in central β and a larger radiation spike of amplitude $P_{rad} \sim$

42 MW. At this time the ICE signal disappears and does not recover subsequently. The large D_α spike is characteristic of a large amplitude ELM, and the reconstructed soft X-ray emission contours show a deformation extending a radial distance ~ 50 cm into the plasma from the edge. A second, large amplitude ELM occurs shortly afterwards at t = 14.18 sec. Similar behaviour was also observed in the pure DD pulse No. 26094. These observations show that a necessary condition for the sudden disappearance of the ICE signal is the occurrence of an ELM of sufficiently large amplitude to perturb the edge plasma significantly in the region of the ICE source. This does not necessarily have to coincide with loss of the central confinement, nor with the roll-over of the neutron emission due to impurity dilution.

4. GENERAL PROPERTIES OF THE EMISSION

4.1 Experimental Constraints on Theoretical Models of Ion Cyclotron Emission

In seeking a plausible emission mechanism for the ICE spectra which are shown, for example, in Figs. 2 and 4, the range of possible theoretical models is strongly constrained by a number of experimental considerations. The evidence from JET discharges with ohmic heating in deuterium, with pure D $\rightarrow$ D NBI, and with mixed D + T $\rightarrow$ D NBI shows that charged fusion products provide the free energy to drive the ICE. However, it is probable that different fusion product species are responsible in each case. The candidate primary DD fusion products from reactions (1) and (2) are: 3 MeV protons, 1 MeV tritons and 0.82 MeV ^3He nuclei; in the 100 % PTE DT case, the dominant fusion product is the 3.5 MeV α-particle produced by reaction (4). In the DT experiments, a diffuse background of DD fusion products is also present, just as in the DD cases there is a diffuse population of energetic α-particles arising from the burn-up of the primary tritium and ^3He products in secondary fusion reactions. The secondary products are, however, produced at a rate significantly lower than that of the primary products. For example, because tritons are born with energies well above the peak in the cross-section for DT reactions, the typical level of tritium burn-up in DD experiments is only of the order of 1 %. It is remarkable that the ICE power spectra in the DD and DT experiments are so similar in form - although very different in relative intensity - given the different reaction rates and concentrations of fusion product of differing species.

A further important constraint on theoretical models arises from the observed spatial localization of the emission at the outer mid-plane edge of the JET plasma, for which there are three independent pieces of evidence. First, the observed frequencies of the spectral lines match the successive deuteron or α-particle cyclotron harmonics at the edge. Second, there are time-resolved observations [6] of ICE sawtooth oscillations which are inverted and show a short time delay with respect to the central sawtooth collapse. Third, the disappearance of

the ICE signal is simultaneous with large amplitude ELMs which penetrate 10 cm - 30 cm into the edge plasma. In addition, the dynamical evolution of the ICE signal is more consistent with the rate of rise of the calculated α-particle density at the edge than at the centre. The band of major radii implied by these observations is 3.9 m $\leq R \leq$ 4.1 m. On general grounds, we note that this narrow band of radii could hardly be smaller in view of the fact that energetic fusion products are responsible for the emission, since the Larmor radii of 3.5 MeV α-particles and of 3 MeV DD fusion protons can be as large as $\rho_\alpha \sim$ 12 cm in the outer edge of the PTE discharges. This implies that the energetic particles responsible for the ICE almost graze the limiter. If their orbital guiding-centres were to be displaced outwards by a distance small compared with the gyroradius, they would strike the limiter surface and promptly be lost from the plasma. Frequency-matching considerations cannot, however, be applied in the analysis of the broad continuum radiation which is dominant above a frequency of about 100 MHz in both DD and DT JET discharges. It is possible that the continuum arises from the overlapping and blending-together of the high l-number emission lines, although we cannot rule out a secondary continuum emission mechanism on the basis of the present experimental results.

The range of possible emission mechanisms is further constrained by the absolute intensity of the ICE. We can compare the measured absolute ICE signal level to the thermal blackbody power emitted by two ion populations in the plasma, namely thermal deuterons with average temperature T_D = 10 keV, and a population of fusion α-particles having a classical slowing-down distribution and effective temperature T_α = 1.3 MeV. If an antenna is placed inside a blackbody enclosure at a temperature T, the blackbody power coupled is P_{BB} = (1/2) $k_B T$ Hz^{-1}, where k_B is Boltzmann's constant, and the factor of 1/2 comes from the fact that any antenna receives only one polarization. From the thermal deuterons we expect P_{BB} = -70 dBm, and from the α-particles, P_{BB} = -50 dBm. Comparing these levels with the data shown in Fig. 5, we see that the most intense ICE signals from the DT discharges exceed the highest value of P_{BB} by a factor of ~ 500, confirming the highly superthermal nature of the ICE. In the present DT discharges, with central α-particle number density $n_\alpha \sim 10^{16}$ m^{-3}, self-absorption is expected to be small; thus the full blackbody level quoted above is unlikely to have been attained in the present experiments.

In our search for a plausible explanation for the measured ICE signals, the above considerations immediately exclude models based on cyclotron radiation from ensembles of charged particles gyrating in the magnetic field. First, even if the plasma were optically thick in this frequency range, we have seen that the observed radiation intensity exceeds the blackbody level by a factor of at least ~ 500. Second, such models would predict radiation from the whole population of energetic ions. Since these are concentrated in the plasma core, they would emit cyclotron radiation in harmonic lines substantially broader and at higher frequencies than those observed. A two-dimensional, full-wave ICRF code has been used to

model the ICE spectrum that would arise if it were appropriate to use the statistics of the local fluctuating current spectrum [15]. These calculations were based on radiation from a slowing-down distribution of energetic fusion products in the plasma core. For simulated JET conditions with a population of fusion α-particles, individual cyclotron harmonic structure is not visible for harmonic numbers $l \geq 2$. This is because, at these high frequencies, more than one harmonic is present in the plasma, giving rise to a broad emission spectrum. It is clear that these predictions are inconsistent with the narrow ICE spectral lines measured on JET. Presumably the ion populations do emit thermal cyclotron radiation, but this must be at an intensity lower than is observed in the experiments. We conclude that a more efficient radiation mechanism must occur at the plasma edge, one which effectively masks any underlying thermal radiation.

We next investigate the detailed structure, in velocity space, of the distribution of the energetic fusion products, paying particular attention to the critical region in the outer edge plasma.

4.2 The Distribution of Fusion Products at the Plasma Edge

The experimental evidence from both ohmic and NBI-heated discharges shows that the superthermal IC line emission originates from fusion products in the outer edge of the plasma. However, the source of DD and DT fusion products has a centrally peaked radial profile which raises the question of how the ICE can be localized in a region where fusion birth is negligible. This problem can be resolved by considering the properties of the drift orbits of the energetic particles. Calculations show the existence of a special class of fusion products, born into trapped orbits in the core plasma, which intersect the outer edge region, defined as $3.9 \text{ m} \leq R \leq 4.1$ m. We have used a single-particle full-orbit code [16] to show that this class lies within a narrow range of trapped pitch angles, just inside the trapped-passing boundary. To illustrate this, in Fig. 14 we show α-particles launched in the magnetic geometry of DT pulse No. 26148 with initial birth position $R_{birth} = 3.46$ m, $\theta_{birth} = 0$. The magnetic axis is at $R_0 = 3.13$ m and the last closed flux surface at $R = 4$ m. Fig. 14(a) shows the passing orbit of an α-particle with a pitch angle of 54.8°, just below the trapped-passing boundary. However, a small increase in the birth pitch-angle to 55.2°, moves the particle into the trapped region, producing the trapped orbit shown in Fig. 14(b). For larger values of the birth pitch-angle, the maximum orbital radius decreases; an example is shown in Fig. 14(c) where the pitch-angle is 65.1°, giving a trapped orbit which does not quite intercept $R = 4$ m. Below the lower limit on the pitch angle at 55.0°, the orbits are passing. For future convenience, let us designate the class of fusion products, which are born in the core plasma and whose drift orbits reach the plasma edge, as large-excursion (LE) particles. Approximately 10 % of the 3.5 MeV α-

particles are of LE type. Orbits of particles born elsewhere in phase space remain close to the plasma core.

Fig. 15 shows the maximum radial excursion of the α-particle guiding centre away from the birth radius, $R_{max} - R_{birth}$, as a function of pitch-angle at birth, $\psi_0 = v_{\|0} / v_{\alpha 0}$, where $v_{\alpha 0}$ is the birth velocity of an α-particle. At this birth position, only those α-particles making radial excursions larger than 0.54 m can reach major radii $R \geq 4.0$ m. It follows that the velocity distribution of the fusion products at the outer mid-plane edge should be exceptionally anisotropic compared with the velocity distribution on the inner flux surfaces. As the LE ions slow down, their orbits contract, so that below a certain energy they no longer intercept the edge. The maximum radial excursions of partially thermalized (2 MeV and 1 MeV) α-particles is also shown in Fig. 15. Only the outermost tips of the Larmor orbits of a fraction of the 2 MeV α-particles can reach $R = 4.0$ m, and none of the 1 MeV α-particles can do so. Thus the region of velocity-space (at $R = 4.0$ m, at the mid-plane) containing the orbits of α-particles is cone-shaped (Fig. 16). The cone is bounded, at the top, by the birth velocity of newly-born α-particles ($v_{\|}^2 + v_{\perp}^2 = v_{\alpha 0}^2$). On the left-hand side is the trapped-passing boundary, and the boundary on the right is determined by the decrease in orbital radius shown in Fig. 15. The edge distribution therefore resembles a *ring* in velocity space and is accordingly maximally anisotropic and non-monotonic.

It is difficult to determine the radial extent of velocity-space anisotropy using this single-particle approach. However, it is possible to treat analytically the broadening effect of the drift orbits on the radial density profile of 3.5 MeV α-particles, in a model [17] where the safety factor is assumed to be independent of radius, and the energetic population divides into two classes: trapped and circulating particles. Applying this model to pulse No. 26148 gives the radial profiles shown in Fig. 17. The plot shows that, at large normalised radii $r/a > 0.8$, in a region of low α-particle production, the density is dominated by trapped particles produced near the plasma core. The excess is balanced by a modest reduction in the α-particle density at smaller radii. This leads naturally to an anisotropic edge velocity distribution in the outer mid-plane of the tokamak. Fig. 17 shows the anisotropy of the α-particle distribution (ratio of trapped-to-untrapped α-particle density). Up to a normalised radius of 0.8 the ratio is close to unity, indicating approximate isotropy. For $r/a > 0.8$, the anisotropy increases dramatically on the low-field side of the torus where the LE orbits, such as the one shown in Fig. 14(b), enhance the local density.

5. ORIGIN OF THE ION CYCLOTRON EMISSION

5.1 Collective Relaxation in the Edge Plasma

In view of the highly superthermal nature of the observed ICE, and its spatial localization in a region of the plasma where the fast ion velocity distribution is likely to be maximally anisotropic and non-monotonic, it is reasonable to seek an explanation for the radiation in terms of collective instability and relaxation. A source of free energy can be made available to drive instabilities from anisotropy

$$\frac{\partial f_\alpha}{\partial v_\perp} \neq \frac{\partial f_\alpha}{\partial v_\parallel}, \tag{7}$$

or non-monotonicity

$$\frac{\partial f_\alpha}{\partial v_\perp} > 0, \tag{8}$$

or radial inhomogeneity

$$\frac{\partial f_\alpha}{\partial r} < 0, \tag{9}$$

of the fast ion velocity distribution function f_α. Each of these features can play a role, together or separately, in destabilizing ion cyclotron instabilities. As we have seen above, each of these terms is likely to be important for the fusion product distribution in the edge plasma.

As a possible explanation of the ICE, in terms of a thermonuclear instability, we consider the excitation of the fast wave Ion Cyclotron Instability (ICI). This can occur even when the concentration of fusion products is small. The essential theoretical feature of the ICI model is the excitation of waves on the fast Alfven and ion Bernstein branches, propagating across the magnetic field with frequencies close to the ion cyclotron harmonics. The relevent literature contains two main approaches, describing closely related physical phenomena, which involve the liberation of free energy from the fast ions to excite the fast Alfven wave in the bulk plasma at cyclotron resonance.

First there are wave-wave models, in which resonance occurs between the fast wave and the negative-energy cyclotron harmonic waves supported by the superthermal ions [18, 19, 20]. In a plasma with a dilute, superthermal ion component, it is possible to excite waves on the fast Alfven-ion Bernstein branch of the the dispersion relation, propagating in the

direction perpendicular to the magnetic field at harmonics of the superthermal and background ion cyclotron frequencies, Ω_α and Ω_i. The real frequency of this instability is given by

$$\omega \cong \omega_0 \equiv c_A k = l\Omega_\alpha, \tag{10}$$

where c_A is the Alfven speed, k is the wavenumber and l is an integer. If $l\ \Omega_\alpha = s\ \Omega_i$ for some integer s, the thermal majority ions give additional positive-energy loading through the resonant ion Bernstein wave that they support. This loading reduces the growth rate of the instability, and determines its threshold. We note that this instability mechanism involves collective excitation driven by *all* the superthermal ions - wave-particle resonance does not arise because $k_{||} = 0$.

The second approach is based on wave-particle resonance ($k_{||} \neq 0$) [21], with the resonance condition given by

$$\omega = l\Omega_\alpha + k_{||} v_{||}. \tag{11}$$

In this approach, only *resonant* fast ions drive the instability. The thermal ions give resonant cyclotron damping; in the limit $k_{||} \rightarrow 0$, this is correctly treated as being negligible in Ref. [21], but no other mechanism which might give rise to a threshold in the absence of cyclotron damping is considered. In particular, the role of resonant cyclotron harmonic waves is not addressed. However, in Ref. [20] the positive-energy loading due to resonant cyclotron harmonic waves at $k_{||} = 0$ is shown to be crucial in determining the threshold. This reflects the fact that, physically, the stabilising influence of the thermal ions ceases to act through the wave-particle cyclotron damping as $k_{||} \rightarrow 0$, but instead acts through cyclotron harmonic wave-wave resonance. The driving term due to the radial inhomogeneity of the fast ion population (Eq.(9)) is included in Ref. [21] where it is shown to be significant, but is not included in the locally uniform model of Ref. [20].

5.2 Linear Wave Analysis of the Ion Cyclotron Instability

We shall follow the wave-wave resonance approach of Ref. [20] and consider only the case of energetic α-particles in a deuterium plasma, so that $\Omega_\alpha = \Omega_i = \Omega_D$ and $l = s$. The dispersion relation has the form

$$\frac{\omega^2 - c_A{}^2 k^2}{\omega^2} = A\xi \frac{\omega}{\omega - l\Omega_\alpha} + B\frac{\omega}{\omega - s\Omega_i}, \tag{12}$$

plus higher order resonances. Here $\xi = n_\alpha / n_i$, where the number densities of the two ion species are n_α and n_i, and the coefficients A and B are complicated functions determined by the velocity-space structure of the ion distributions. Details are given in [19, 20]. Physically, instability arises in Eq.(12) through resonance between the fast Alfven wave branch (left hand side) and cyclotron harmonic waves (right hand side) supported by the energetic ions (negative-energy driving mechanism) and background ions (positive-energy loading). Before presenting the results of a numerical solution of the full dispersion relation, it is instructive to consider the analytical approximation which arises in the limit of $\omega^2 >> \Omega_i^2$, provided certain conditions are satisfied. If the concentration of energetic ions, the plasma beta, and the ratio c_A / c are all small, it can be shown that $\Delta\omega$ ($\equiv \omega - \omega_0$) for a monoenergetic minority ion distribution is given by [19, 20]

$$\frac{\Delta\omega^2}{\omega_0^{\,2}} = \frac{1}{2\omega_{pi}^{\,2}}\left[\omega_{p\alpha}^{\,2}\frac{c_A^{\,2}}{v_0^{\,2}}\chi_0^{\,2}(z_\alpha) + \omega_{pi}^{\,2}\frac{s^2}{z_i^{\,2}}I_s(z_i^{\,2})\exp(-z_i^{\,2})\right], \tag{13}$$

where $\omega_{p\alpha}$ and ω_{pi} are the plasma frequencies of the two ion species, v_0 is the (unique) speed of the minority ions, and

$$z_\alpha = \frac{kv_0}{\Omega_\alpha} = l\frac{v_0}{c_A}, \tag{14}$$

and

$$z_i^{\,2} = \frac{k^2 v_i^{\,2}}{2\Omega_i^{\,2}}, \tag{15}$$

where v_i is the majority ion thermal speed. The function χ_0^2 is a function of z_α which depends on the velocity space distribution of minority ions (see below), and I_s is the modified Bessel function of the first kind of order s. χ_0^2 can be positive or negative, depending on the value of z_α, whereas $I_s(z_i^2)$ is always positive. Instability occurs if the right hand side of Eq.(13) is negative, in which case the growth rate is $|\Delta\omega|$. If $\chi_0^2 < 0$, there is a threshold concentration of minority ions above which the l-th harmonic will be excited [20]. We find that the minority ion concentration required for instability is

$$\xi_{crit} = -\frac{1}{\chi_0^{\,2}} \frac{m_i}{m_\alpha} \frac{z_\alpha^{\,2}}{z_i^{\,2}} I_s(z_i^{\,2}) \exp(-z_i^{\,2}), \tag{16}$$

where m_α and m_i are the corresponding ion masses and we recall $s = l$ for α-particles in deuterium. In the limit $v_i \rightarrow 0$ we find that $\xi_{crit} \rightarrow 0$, and

$$\frac{\Delta\omega}{\omega_0} = \frac{1}{\sqrt{2}} \frac{\omega_{p\alpha}}{\omega_{pi}} \frac{l}{z_\alpha} \chi_0(z_\alpha). \tag{17}$$

In this equation we have used the second equality in Eq.(14).

5.3 Criteria for Instability in JET

In section 4.2, we saw that the LE energetic ion distribution in the edge plasma forms a ring in velocity space. We have approximated the ring distribution analytically by the function $f_\alpha \propto \delta(v_\parallel)\, \delta(v_\perp - v_{\perp 0})$, from which it can be shown that

$$\chi_0^{\,2} = z_\alpha \frac{dJ_l^{\,2}}{dz_\alpha} - \frac{2z_\alpha}{ls} \frac{d}{dz_\alpha}\left(z_\alpha J_l \frac{dJ_l}{dz_\alpha}\right) + \frac{z_\alpha}{l^2 s^2} \frac{d}{dz_\alpha}\left(z_\alpha^{\,2}\left(\frac{dJ_l}{dz_\alpha}\right)^2\right), \tag{18}$$

where J_l is the Bessel function of order l. In the JET edge plasma, the relevant particle densities fall off rapidly with radial distance, as shown in Fig. 6. It is therefore logical to plot ξ_{crit} as a function of n_i for various values of l, with $-z_\alpha^{\,2} / \chi_0^{\,2}$ set equal to its minimum value, taking the edge ion temperature as T_i = 1 keV. The critical α-particle concentration required for exciting the second, third and fourth cyclotron harmonics is shown in Fig. 18. Allowing for the effects of finite α-particle Larmor radius and the poloidal asymmetry as discussed above for the conditions of Fig. 6, we estimate the local value of ξ to be of the order of 10^{-4} in the outer mid-plane edge plasma. Fig. 18 implies that this concentration of ring ions is sufficient to excite cyclotron harmonics with $l \geq 3$. In the case of $l = 2$, instability cannot occur unless a significant number of α-particles reach the outermost region, in which n_i is of the order of 10^{18} m^{-3} or less.

It should be stressed that the threshold concentrations shown in Fig. 18 represent necessary but insufficient conditions for instability. The sign of $\Delta\omega^2$ also depends on z_α, and hence on v_0. Taking edge values of B = 2.1 T, $n_i \leq 2.1 \times 10^{19}$ m^{-3} and α-particles with energies of 3.5 MeV, we find that

$$\frac{v_0}{c_A} \leq 1.83, \tag{19}$$

which means that $z_\alpha \leq 3.66$ for $l = 2$ and $z_\alpha \leq 5.49$ for $l = 3$. Evaluating $- \chi_0^2 / z_\alpha^2$ as a function of z_α for $l = 2$ reveals that instability occurs only for values of z_α considerably higher than 3.66. In its present form, the model cannot, therefore, account directly for the observed excitation of ICE for the two lowest harmonics $\omega \cong \Omega_\alpha$ and $\omega \cong 2\ \Omega_\alpha$. For $l = 3$, on the other hand, we find that $- \chi_0^2 / z_\alpha^2 > 0$ for $z_\alpha = 5.49$ so that instability is possible in this case.

So far we have considered only the conditions necessary for linear growth of the ion cyclotron instability. The growth rate of unstable waves has been calculated for JET conditions [20]. However, the linear growth rates of different harmonics do not necessarily correlate with the intensities of the corresponding ICE lines, since it is likely that the latter are determined by some nonlinear saturation process. The situation may be further complicated by the presence of energetic protons in the edge plasma, and the consequent excitation of proton cyclotron harmonics. The presence of such protons could explain, incidentally, the observed excitation of the $l = 2$ line. Linear analysis of both unstable shell and ring distributions in simulated JET DD fusion conditions with low ($\xi \sim 10^{-5}$) concentrations [20] indicates that, of the DD fusion products, only 3 MeV protons give instability; whereas the 0.8 MeV ^3He and 1 MeV tritons lie below threshold.

The present analysis, however, omits the driving term (Eq.(9)) arising from the spatial inhomogeneity of the fast ion distribution at the edge of the plasma. It follows from the work of Ref. [21] that the additional operator associated with the fast ion density gradient and the primary operator associated with the velocity-space gradient are in the ratio

$$\frac{\omega_{*\alpha}}{\omega} \cong \frac{k_y v_\alpha^{\ 2}}{\omega \Omega_\alpha L_{n\alpha}} \cong \frac{1}{l} \frac{\rho_\alpha}{L_{n\alpha}} k_y \rho_\alpha . \tag{20}$$

Here $\omega_{*\alpha}$ is a diamagnetic frequency, k_y is the poloidal wavenumber, v_α the velocity of the energetic ions, and $L_{n\alpha} = -(d \ln n_\alpha / dr)^{-1}$ is the lengthscale associated with the density inhomogeneity of the energetic ions. Fig. 19 shows that the ratio $\rho_\alpha / L_{n\alpha}$ comes close to unity in the JET edge plasma, whereas it is to be expected that $k_y \rho_\alpha$ would be small compared with unity. It therefore follows from Eq.(20) that density inhomogeneity may enhance the instability driving term, particularly at low l-values, in a way which may be significant at marginal stability. The exact magnitude of this term depends, in general, on the nature of the mode excited and on the velocity-space structure of the energetic ions.

As it stands, the ICI model is capable only of predicting the excitation of modes with frequencies close to the harmonics of the cyclotron frequencies of the energetic species. In pure deuterium fusion experiments, the 3 MeV fusion proton arising from reaction (2) is a likely candidate to drive instability. In this case, the ICI model cannot explain the direct excitation of the observed ICE lines with frequencies which coincide with the odd deuteron harmonics $\omega \cong l\,\Omega_D$ (l = 1, 3, 5, ...). However, in all cases, a deuterium background plasma is present. To explain the DD ICE spectra, it may therefore be appropriate to invoke a nonlinear energy coupling mechanism, leading to equipartition of energy between modes, that results in additional spectral peaks at odd-numbered harmonics of the deuteron cyclotron frequency, supported by the deuterium background. The similar forms of ICE spectra observed in DD and DT plasmas could possibly arise by this process. Thus deuterium cyclotron harmonics would always be excited in a bulk deuterium plasma, irrespective of whether the driving particle is a 3 MeV proton (in the DD fusion case) or a 3.5 MeV α-particle (in the DT case). Moreover, if some form of nonlinear coupling mechanism were present, this could provide a natural explanation for the observed l = 1 and l = 2 deuterium cyclotron harmonics. On this interpretation, these harmonics would not be directly excited in the instability, but could be indirectly excited by the flow of energy from other ($l \geq 3$) modes which are directly excited.

Clearly, however, the linear theory of ICI is not yet fully developed. For example, in a complete theory, the inclusion of small $k_{||} << k_{\perp}$ will reduce the positive-energy loading while increasing cyclotron damping relative to $k_{||} = 0$. It is possible that, when fully quantified, this will lead to a net lowering of thresholds.

6. DISCUSSION

We have noted fluctuations in ion cyclotron emission, whose amplitude is of order 100 % and which are spatially coherent over a radial range $\Delta R \sim 20$ cm. For JET plasma parameters, the ICI model predicts linear growth rates $\gamma / \omega \sim 10^{-4}$, implying $\gamma \sim 10$ kHz and suggesting that the mode can be switched on at a rate which exceeds the data sampling rate of 2 kHz. Turning to the switch-off, two possible mechanisms may operate. First, the threshold condition in the ICI model is sensitive to small variations in a number of local parameters, for example v_α / c_A. Near threshold, relatively small fluctuations in plasma density (and therefore c_A) would switch the mode on or off, giving rise to a bursting type of behaviour. In this case, we would expect the ICE and edge plasma fluctuations to be temporally correlated. The relevant edge plasma fluctuations would need to have perpendicular wavevectors smaller than ~ 30 m^{-1}, in order to maintain coherence. A second explanation of the bursting behaviour is mode switch-off, due to nonlinear effects, once the instability reaches some critical saturated amplitude.

The ICI model may also be consistent with observation of the disappearance of the ICE signal, correlated with the large amplitude ELMs. If a large ELM expels energetic ions from an outer plasma region of thickness approximately 30 cm, the LE population will temporarily be annihilated, leading to the observed extinction of the ICE signal. However, the central birth of fusion ions continues and is sufficient to re-build the fast ion population to a level at which the instability can be triggered again after the ELM. Thus the ICE signal returns after a delay, which we noted in Section 3.2.2 is approximately 20 ms. To explain this delay, we estimate the time taken to replace completely the ring of LE ions in velocity-space. First consider the time taken for α-particles, freshly-born into LE orbits, to diffuse in energy from their initial birth energy $E_{\alpha 0}$ to a final energy $E_{\alpha 0}$ - ΔE_α. The decrement ΔE_α is equivalent to the energy-width of the ring shown in Fig. 16: α-particles slowing down by ion-electron collisions move radially in velocity-space. The time taken for the ring to be refilled with energetic α-particles is given by

$$\Delta t_s \approx -\ell n\left(1-\frac{\Delta E_\alpha}{E_{\alpha 0}}\right)\frac{\langle \tau_s \rangle}{2}, \tag{21}$$

where $\langle \tau_s \rangle$ is the momentum slowing-down time of the α-particle due to collisions with electrons, averaged over its trapped orbit. During the period of intense large-amplitude ELM activity in pulse No. 26148, the TRANSP simulation allows us to estimate $\langle \tau_s \rangle \sim 300$ ms. Taking the energy-width of the ring to be in the range $\Delta E_\alpha = 0.5$ MeV - 1.0 MeV, we predict the refilling time of the ring to be in the range $\Delta t_s = 23$ ms - 50 ms, close to the observed delay. Partial filling of the ring may be sufficient to produce unstable structures in velocity-space, which would form on timescales at the lower end of this range. The ring may, however, also be replenished by pitch-angle scattering of energetic α-particles from adjacent orbits in the passing region, close to the trapped-passing boundary, as shown in Fig. 14(a). To refill the ring by this process, the passing particles would need to be scattered in pitch-angle by an amount of the order of the pitch-angle width of the ring, $\Delta\psi \sim 20°$. This process would take a time

$$\Delta t_{pa} \approx \left(\frac{2\Delta\psi}{\pi}\right)^2 \langle \tau_{\pi/2} \rangle, \tag{22}$$

to complete where $\langle \tau_{\pi/2} \rangle$ is the average time for an energetic α-particle to be scattered through a pitch angle of π / 2. During the period of the ELM activity in pulse No. 26148, the TRANSP simulation gives values of $\langle \tau_{\pi/2} \rangle$ in the range 20 sec - 40 sec, and a corresponding range $\Delta t_{pa} = 1$ sec - 2 sec. Thus it is unlikely that classical pitch-angle scattering collisions alone can re-populate the ring on the observed timescale of ~ 20 ms.

The observed correlation of ICE with inverted sawteeth can also be interpreted in a complementary way. Following the central sawtooth collapse, a local enhancement of fusion reactivity occurs as the heat pulse propagates outwards. In the region just exterior to the sawtooth inversion radius, the heat pulse will produce a temporary enhancement in reactivity and therefore of the LE population, resulting in a pulse of ICE correlated with the inverted sawtooth. We noted above that in the PTE series of discharges, with plasma current $I_p = 3.1$ MA, the ICE-sawtooth correlations were not as clear as those observed in the earlier series of high current discharges. This may be connected with the fact that the sawtooth inversion radius in the PTE discharges is smaller ($r/a \sim 0.33$) than in the earlier high current ohmically heated discharges ($r/a \sim 0.58$), so that the influence of sawteeth on the LE population is weaker. Fom MHD observations we note, in addition, that outer modes with $m > 1$ can have a relatively stronger effect on the ICE compared with central modes.

Let us now turn to an interesting null observation: the apparent absence of ICE from the plasma centre. If ICE is driven by velocity space instability, the conditions for some form of population inversion must be satisfied in the emitting region. However, it may be impossible to meet these conditions in the plasma centre. For example, it has been noted [6, 22, 23] that, if the fusion reactivity increases sufficiently rapidly, it can generate an unstable shell-type fusion product population. In the PTE experiments, however, the rate of rise of the fusion reactivity, R_{DT}, (Fig. 7) is insufficient to satisfy the criterion for velocity-space population inversion [22, 23]

$$\tau_s \frac{1}{R_{DT}} \frac{\partial R_{DT}}{\partial t} \geq 3 - \nu_{loss} \tau_s, \tag{23}$$

unless the α-particle loss frequency, ν_{loss} , is significant. In the edge plasma, ν_{loss} may be sufficiently large for the inequality Eq.(23) to be satisfied; but in the plasma centre, we expect ν_{loss} to be negligible. Hence unstable shell-type distributions can be generated more easily in the edge plasma than in the plasma centre. This is consistent with the fact that ICE from the plasma centre is not observed. Marginal satisfaction of Eq.(23) during the rapid heating phase allows us to place an upper limit on the value of $\nu_{loss} \sim 6\ s^{-1}$.

The width of the spectral lines is limited by the radial extent of the source region. As we have discussed, the most likely driving mechanism appears to be velocity-space anisotropy arising from drift orbit excursions. Fig. 17 shows that significant anisotropy is confined to the region $0.8 \leq r/a \leq 1.0$. Given the inverse dependence of local cyclotron frequency on major radius, it follows that this radial range corresponds to a frequency range

$$\Delta\nu / \nu \approx 0.2\, a / R_{edge} \approx 0.06, \tag{24}$$

which is close to the observed spectral linewidth $\Delta\nu / \nu \approx 0.09$. The small size of the difference between the observed spectral linewidth and that obtained from Eq.(24) places a constraint on the magnitude of any additional broadening mechanism.

The fine structure of the low-l ICE lines is a new feature of the present observations. We recall from Section 3.1 that the lines are split into blended doublet or triplet shapes with linewidth $\Delta\nu / \nu \sim 0.06$. This may be due to poloidal field or diamagnetic effects. Adam and Jacquinot [24] have pointed out the existence of fine-structure in the global fast wave modes in a tokamak, which arises from the interaction of the poloidal field with the toroidal plasma current. This produces a small energy shift between co-propagating and counter-propagating waves. The magnitude of the splitting, $\Delta n_{\|} \sim (c / \omega r)(B_\theta / B)$, corresponds to $\Delta k_{\|} \sim 0.1$ m^{-1} in the present case. Given that the acceptance range of the antenna is $0 \leq | k_{\|} | < \sim 7$ m^{-1}, it is clear that $\Delta k_{\|} / | k_{\|} | \sim \Delta\nu / \nu \sim 0.06$ would be compatible with existing data. We also note that this frequency splitting is comparable in magnitude to the inhomogeneity drift frequency of the energetic ions, ω_{di}, suggesting that the superposition of collective modes with relative frequencies $\pm \omega_{di}$ may be responsible. For radially localised modes of the type discussed in Ref. [21], this term can be interpreted as referring to the two waves (travelling in the $\pm z$-directions) needed to form the mode. As l increases, the splitting also increases, and the lines eventually overlap at sufficiently large l, forming a continuum. Complete overlap of the lines would occur at a frequency $\nu \sim 100$ MHz, close to the frequency of the onset of the observed continua in JET and in TFTR.

It is instructive to consider how the maximum radial displacement of each of the DD fusion products scales with initial perpendicular energy, $E_{\perp 0}$. The maximum minor radial excursion is given by $r_{max} \propto \rho_\theta^{2/3} \propto (A_\alpha E_{\perp 0})^{1/3} / Z_\alpha^{2/3}$, where ρ_θ is the poloidal Larmor radius, and A_α and Z_α are the atomic mass and atomic number of the fusion product. For the set of DD fusion products {proton (3 MeV), triton (1 MeV), ^3He (0.82 MeV)}, we calculate the set of ratios r_{max}(DD product) / r_{max}(3.5 MeV α-particle) to be {0.95, 0.95, 0.56}. This shows that it is possible only for the protons and tritons to follow LE orbits; the ^3He ions have insufficient birth energy to reach the JET plasma edge. We recall that ICE lines with frequencies at ^3He cyclotron harmonics have been observed in TFTR experiments, but not in JET. The larger poloidal Larmor radii expected in TFTR, which has lower plasma current than JET, may allow the ^3He fusion ions to reach the edge plasma and give rise to the observed ^3He ICE lines.

The present ICE results are also of interest in the context of current theoretical investigations of collective α-particle instabilities, in particular, the toroidicity-induced Alfven eigenmodes (TAEs) [25, 26]. The TAEs are discrete MHD modes appearing near the Alfven frequency, which can be resonantly destabilized by circulating and trapped α-particles when the α-particle radial pressure gradient is sufficiently steep and β_α is sufficiently large. In the DT pulse No. 26148, the predicted TAE mode frequency is in the range 100 kHz - 300 kHz.

It has been suggested that excitation of such modes can lead to loss or radial redistribution of the energetic ions. The theoretical boundary for the destabilization of TAE modes has been computed for realistic tokamak conditions [27] and depends primarily on the magnitude of the volume averaged toroidal beta, $\langle \beta_\alpha \rangle$, and the ratio $v_{\alpha 0} / c_A$, where $v_{\alpha 0}$ is the α-particle birth velocity. Details of the threshold also depend on the ratio of the lengthscale of the α-particle pressure, $L_\alpha = -(d \ln \beta_\alpha / dr)^{-1}$ to the plasma minor radius, a. From the theoretical literature we note, however, that there is considerable uncertainty in the precise location of the instability boundary. Using the TRANSP Monte-Carlo α-particle results for DT pulse No. 26148 (at time = 13.2 sec, near the peak of the DT fusion production), we find maximum values of $L_\alpha / a \sim 0.35$, $v_{\alpha 0} / c_A \sim 1.8$ and $\langle \beta_\alpha \rangle \cong 1.42 \times 10^{-4}$. These values have been compared with the theoretical TAE instability boundary [12] showing the JET data to lie marginally in the stable region. This is due, primarily, to the large ratio of $v_{\alpha 0} / c_A$. Values of this ratio closer to unity would have implied instability. This result is consistent with the observation that the integrated ICE signal in this discharge (Fig. 8) simply increases in proportion to the calculated α-particle density up to the time of the X-event. There is no evidence for saturation in the ICE signal which might have been attributable to anomalous α-particle losses.

The origin of the MHD mode shown in Fig. 11 is unknown. Although it preceeds the ELM, it is not typical of other ELM precursors which have been observed [14]. However, the low frequency of this mode (4.5 kHz) makes it unlikely to be of TAE or fishbone type. The fact that this mode has been observed only in the two DT discharges (pulse Nos. 26147 and 26148) where its destabilisation coincides with the growth of the ICE signal, might indicate that it is triggered by fusion α-particles. Future DT experiments will enable us to test this hypothesis.

In this paper, we have seen how ICE has provided a diagnostic for fusion α-particles in the Preliminary Tritium Experiment on JET. No other diagnostic system has yet been able to fulfil this role.

ACKNOWLEDGEMENTS

It is a pleasure to thank the many JET Team members involved in the PTE experimental campaign from the Operations, Heating and Diagnostic groups. We also thank Andy Sibley and Martin Schmid for technical advice, Piet van Belle for help with running the JET single-particle orbit code, and Bernard Balet and Pam Stubberfield for their help with the TRANSP α-particle Monte-Carlo code. We also thank Duarte Borba and Shakeib Ali-Arshad for help

with the MHD analysis, Jim Hastie and Chris Lashmore-Davies for helpful discussions, and Ken McClements for computation of Figure 18.

REFERENCES

[1] The JET Team, The JET Project - Design Proposal, Rep. EUR-JET-R5, CEC, Brussels (1975).

[2] COTTRELL, G.A., LALLIA, P.P., SADLER, G. and VAN BELLE, P., (Proc. 13th EPS Conf. '*Controlled Fusion and Plasma Heating*', Schliersee, Germany 1986) Vol **10C**, part **II** (1986) 37.

[3] CLARK, W.H.M., (Proc. 4th Int. Symp. '*Heating in Toroidal Plasmas*' , Rome, 1984) **I**, EUR 9341 EN (1984) 385.

[4] COTTRELL, G.A., (Proc. Course and Workshop on Applications of RF Waves to Tokamak Plasmas. Ed. Bernabei, S., Gasparino, U and Sindoni, E., Varenna, 1985) EUR 10333 EN **II** (1985) 710.

[5] COTTRELL, G.A. & DENDY, R.O., *Phys. Rev. Lett.* **60** (1) (1988) 33.

[6] SCHILD, P., COTTRELL, G.A. & DENDY, R.O., *Nuclear Fusion Lett.* **29** (5) (1989) 834.

[7] GREENE, G.J., et al., (Proc. 17th EPS Conf. '*Controlled Fusion and Plasma Heating*', Amsterdam, The Netherlands, 1990) Vol **14B**, part **IV** (1990) 1540.

[8] YOUNG, K., TFTR, private communication (1992).

[9] THE JET TEAM, *Nuclear Fusion* **32** (2) (1992) 187.

[10] COTTRELL, G.A., BHATNAGAR, V.P., DA COSTA, O., et al., (Proc. 19th EPS Conf. '*Controlled Fusion and Plasma Heating*', Innsbruck, Austria, 1992) Vol **16C**, part **I** (1992) 327.

[11] GOLDSTON, R.J., McCUNE, D.C., TOWNER, H.H. et al., J.Comput. Phys. **43** (1981) 61.

[12] BALET, B., STUBBERFIELD, P.M., CORDEY, J.G., et al., *Nuclear Fusion*, in preparation (1992).

[13] CAMPBELL, D., et al., *Nuclear Fusion*, in preparation (1992).

[14] ALI-ARSHAD, S., CAMPBELL, D., COLTON, A., et al., (Proc. 19th EPS Conf. '*Controlled Fusion and Plasma Heating*', Innsbruck, Austria, 1992) Vol **16C**, part **I** (1992) 227.

[15] BATCHELOR, D.B., JAEGER, E.F. and COLESTOCK, P.L., *Phys. Fluids B* **1** (6) (1989) 1174.

[16] VAN BELLE, P., JET, private communication (1992).

[17] STRINGER, T.E., *Plasma Phys.* **16** (1974) 651.

[18] MIKAILOVSKII, A.B., in **Reviews of Plasma Physics** (ed. by M.A.Leontovich, Consultants Bureau, New York, 1986), Vol. 9, p.103.

[19] BELIKOV, V.S. and KOLESNICHENKO, Ya. I., Sov. Phys. Tech. Phys. **20**, (1976) 1146.

[20] DENDY, R.O., LASHMORE-DAVIES, C.N. and KAM, K.F., *Phys. Fluids* **B 4** (1992), accepted for publication.

[21] COPPI, B., COWLEY, S.C., KULSRUD, R., et al., *Phys. Fluids* **29** (12) (1986) 4060.

[22] SIGMAR, D., (Proc. Physics of Plasmas Close to Thermonuclear Conditions, Varenna, 1979) **I**, CEC Brussels (1979) 271.

[23] CORDEY, J.G., GOLDSTON, R.J. and MIKKLESON, D.R., *Nuclear Fusion*, **21** (5) (1981) 581.

[24] ADAM, J., JACQUINOT, J., Report EUR-CEA-FC-886 (1977).

[25] CHEN, L., in Theory of Fusion Plasmas (Proc. Joint Varenna-Lausanne Int. Workshop Chexbres, 1988) Editrice Compositori, Bologna (1989) 327.

[26] CHENG, C.Z., *Phys. Fluids* **B 3** (1991) 2463 and references therein.

[27] BUDNY, R.V., BELL, M.G., BIGLARI, H., et al., *Nuclear Fusion*, **32** (3) (1992) 429.

Table I

JET PTE DT parameters: (pulse No. 26148 at time = 13.2 sec). Parameters from TRANSP simulation, including those based on the Monte-Carlo α-particle model, are designated by an asterisk.

Plasma Current, I_p	3.1 MA
Toroidal Field, B_T	2.8 T
Central Electron Density, $n_e(0)$	3.6×10^{19} m^{-3}
Injected D neutral beam power	12.8 MW
Injected T neutral beam power	1.5 MW
*Central (D + T) ion density, $n_i(0)$, (thermal)	2.0×10^{19} m^{-3}
*Ratio: average T to average (D + T) density (thermal)	0.13
Central Electron Temperature, $T_e(0)$	9.9 keV
Central Ion Temperature, $T_i(0)$	18.8 keV
Diamagnetic stored energy	9.1 MJ
Total Neutron Flux	6×10^{17} s^{-1}
Fusion Power	1.7 MW
Central Larmor radius of 3.5 MeV α-particle, $\rho_\alpha(0)$	9.7 cm
Central Alfven velocity, $c_A(0)$	7.08×10^6 m s^{-1}
α-particle birth velocity, $v_{\alpha 0}$	1.3×10^7 m s^{-1}
Ratio: $v_{\alpha 0} / c_A(0)$	1.83
*Volume averaged toroidal α-particle beta, $\langle \beta_\alpha \rangle$	1.42×10^{-4}
*Central toroidal α-particle beta, $\beta_\alpha(0)$	1.36×10^{-3}
*Ratio: $n_\alpha(0) / n_e(0)$	7.8×10^{-4}
*Central α-particle slowing-down time, $\tau_\alpha(0)$	1.03 sec
*α-particle power to electrons, $P_{\alpha e}$	210 kW
*α-particle power to ions, $P_{\alpha i}$	25 kW

Table II

Comparison of measured ICE power with neutron flux for two PTE discharges having similar magnetic configuration and neutral beam injection power. Discharge a) was run with pure deuterium neutral beam injection; in discharge b), tritium was introduced from two injectors delivering 1.44 MW at 78 keV, and the remaining injectors were run with pure deuterium.

Case	**Pulse No. (time)**	P_{NBI} **(MW)**	P_{ICE} **(ν = 33 MHz)**	**Neutron flux** ($\times 10^{16}$ s^{-1})
a	26094 (13.2)	13.2	0.12 μW	2.7
b	26147 (13.2)	14.4	3.1 μW	53
Ratio: *b* / *a*		1.09	26	20

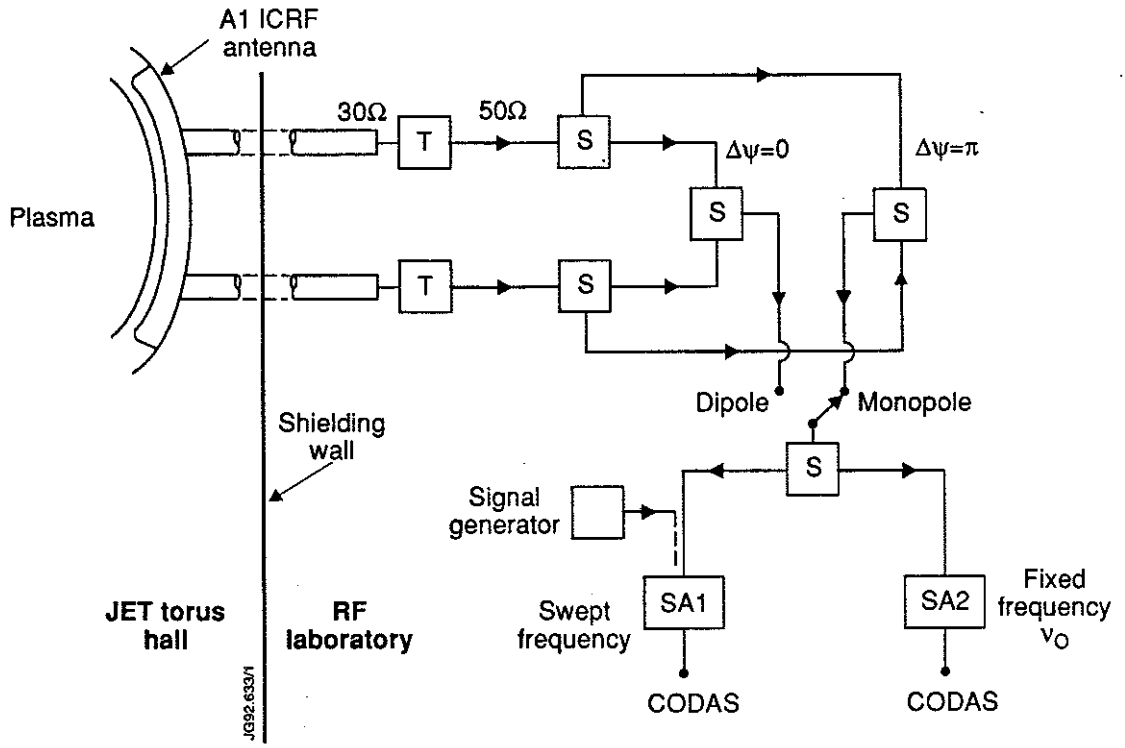

Fig 1: Experimental arrangement used to make ICE measurements on JET tritium experiment discharges. The circuit elements marked 'T' are impedance matching transformers; those marked 'S' are power splitters. CODAS refers to the JET data acquisition system.

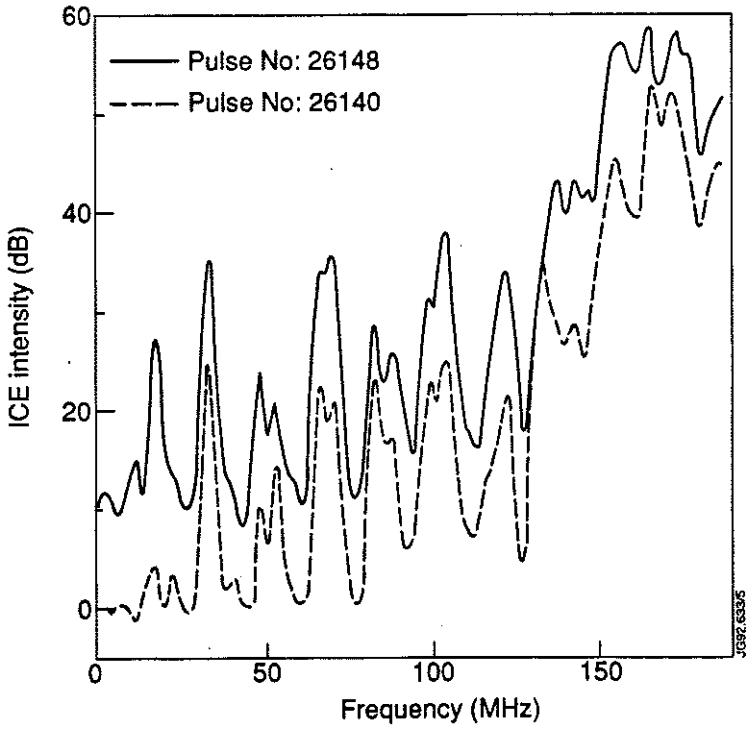

Fig 2: ICE spectra measured in DT and DD discharges. DT: solid curve, pulse No. 26148; DD: dashed curve, pulse No. 26140. In both cases, a monopole antenna was used and the data were taken close to the time of the peak neutron emission. The noise floor was at 0 dB for pulse No. 26140 and at + 10 dB for pulse No. 26148.

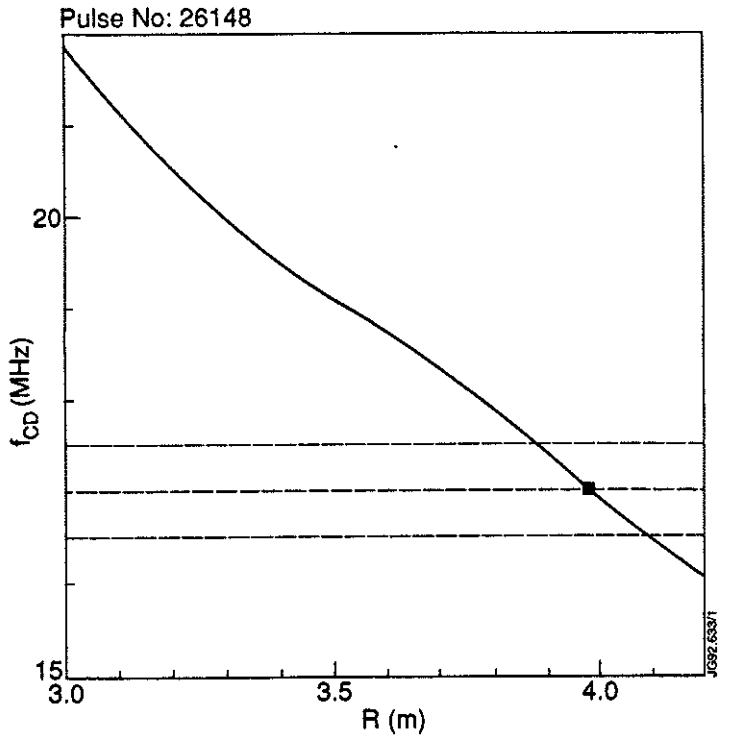

Fig 3: The cyclotron frequency of deuterons (degenerate with α-particles) in the total magnetic field as a function of major radius for DT pulse No. 26148. The central horizontal dashed line represents the frequency spacing between the centres of the ICE spectral lines; the intercept shows the radius with matching cyclotron frequency. The upper and lower dashed lines represent the error limits in the measurement of the frequency spacing of the lines.

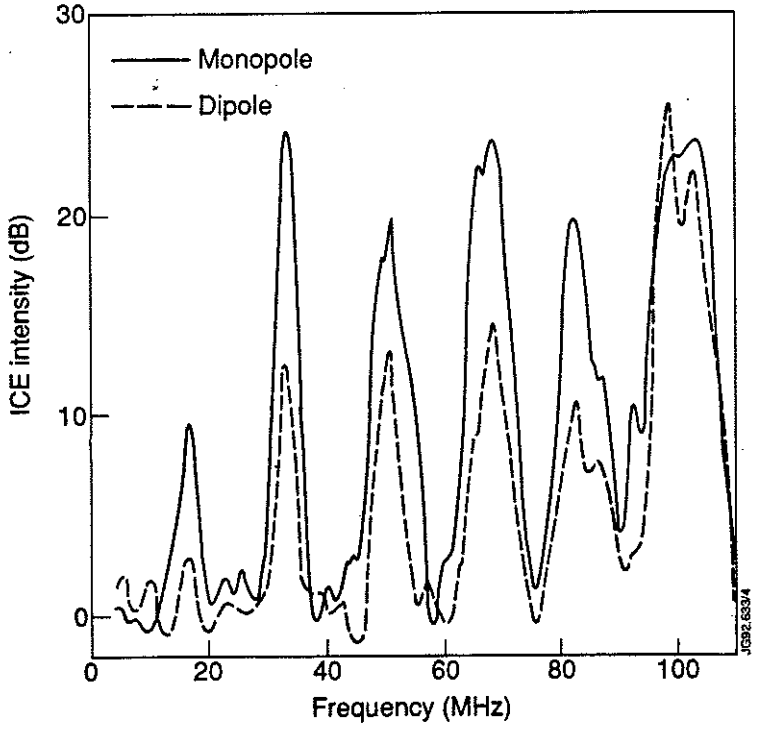

Fig 4: Comparison of ICE spectra measured in similar NBI discharges with 1 % tritium for monopole (solid curve, pulse No. 26095) and dipole (dashed curve, pulse No. 26108) antenna configurations.

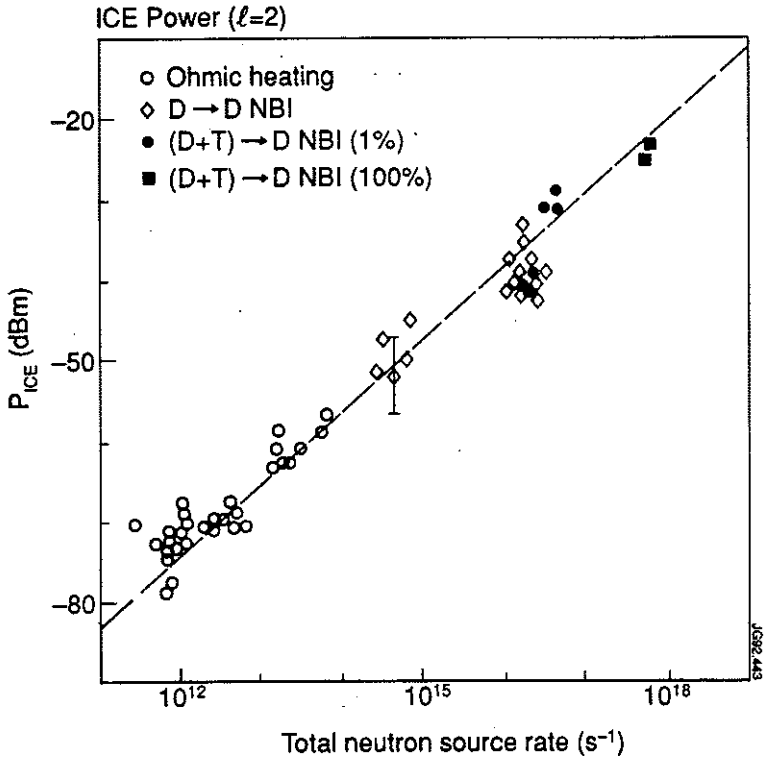

Fig 5: Correlation between ICE intensity P_{ICE} and total neutron emission rate R_{NT} for ohmic and NBI heated JET discharges, over six decades of signal intensity. The best fitting relation is $P_{ICE} \propto R_{NT}^{0.9\pm0.1}$.

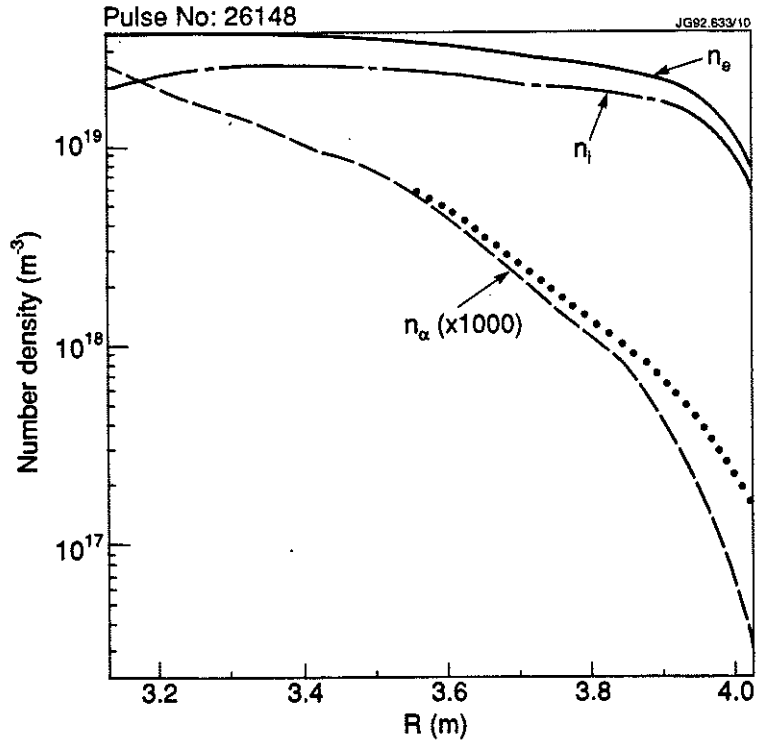

Fig 6: Radial density profiles for ions, electrons and α-particles in DT pulse No. 26148 at time t = 13.2 seconds. The α-particle density was computed from a model based on guiding-centre orbital trajectories, averaged over each flux surface. The dotted curve shows the effect on the α-particle density profile of the broadening due to the finite Larmor radius of the α-particles.

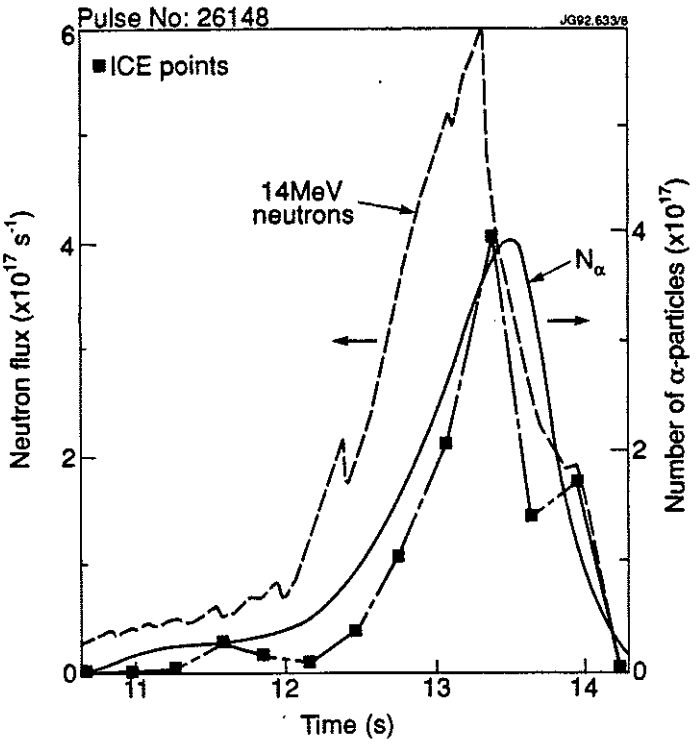

Fig 7: Time-evolution of the 14 MeV neutron emission R_{DT} and total number of α-particles (solid line), compared with the integrated ICE signal (points) for DT pulse No. 26148.

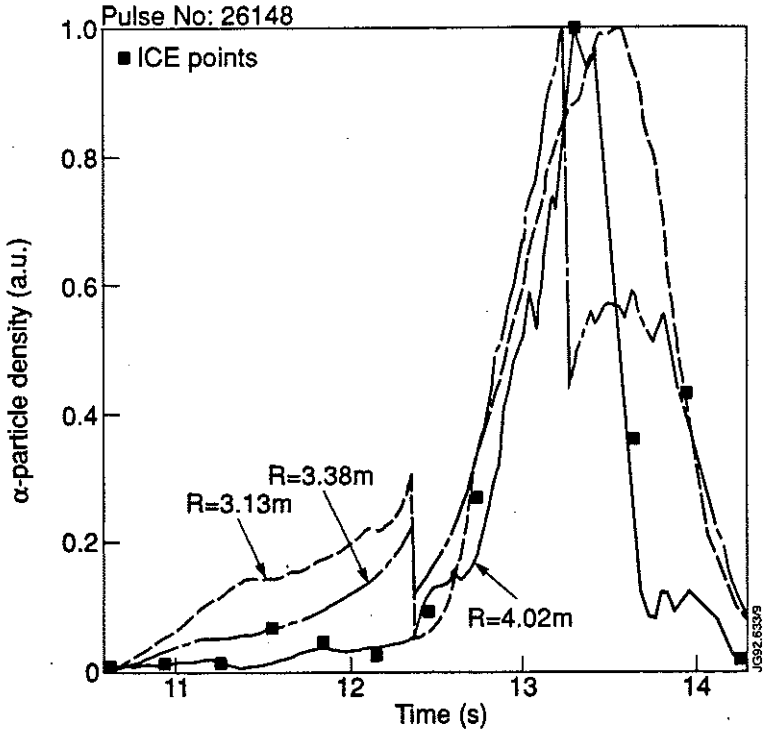

Fig 8: Time-evolution of the α-particle density at selected radii, compared with the integrated ICE signal (points) for DT pulse No. 26148.

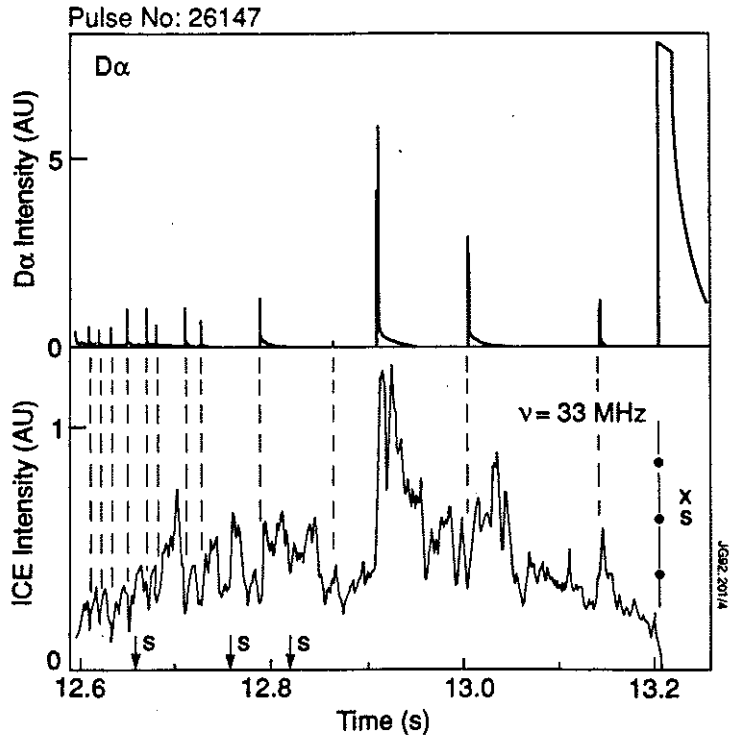

Fig 9: Comparison of the ICE signal with ELM events showing correlation prior to the X-event, for DT pulse No. 26147. The times of sawtooth collapse are denoted by the symbols 'S', and the X-event and associated sawtooth collapse by 'XS'.

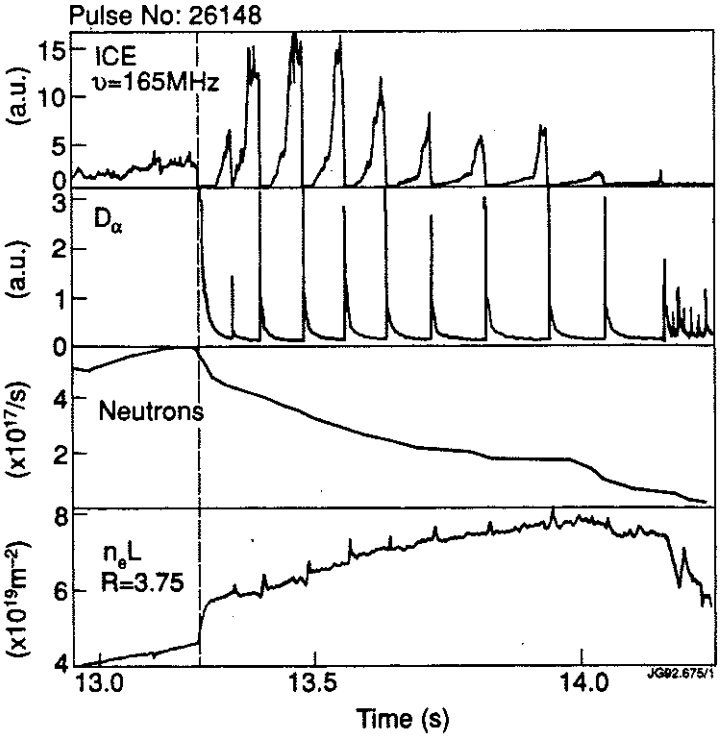

Fig 10: The termination phase of DT pulse No. 26148, showing the correlation with ELMs of the ICE, a D_α signal, the total DT reaction rate R_{DT}, and the electron density integrated along a line-of-sight tangent to the flux-surfaces at R = 3.75 m. The X-event occured at time t = 13.28 seconds, shown by the vertical dashed line.

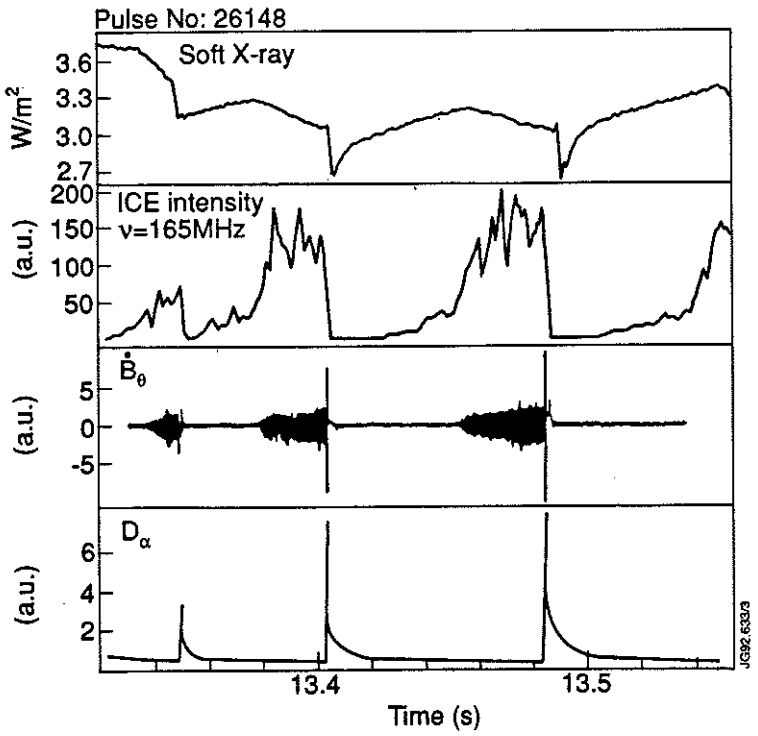

Fig 11: Time-expanded view of the termination phase of DT pulse No. 26148, showing details of the correlation with ELMs of the ICE, a D_α signal, an MHD coil mounted at the top of the vessel, and a soft X-ray line-of-sight at major radius $R = 3.98$ m.

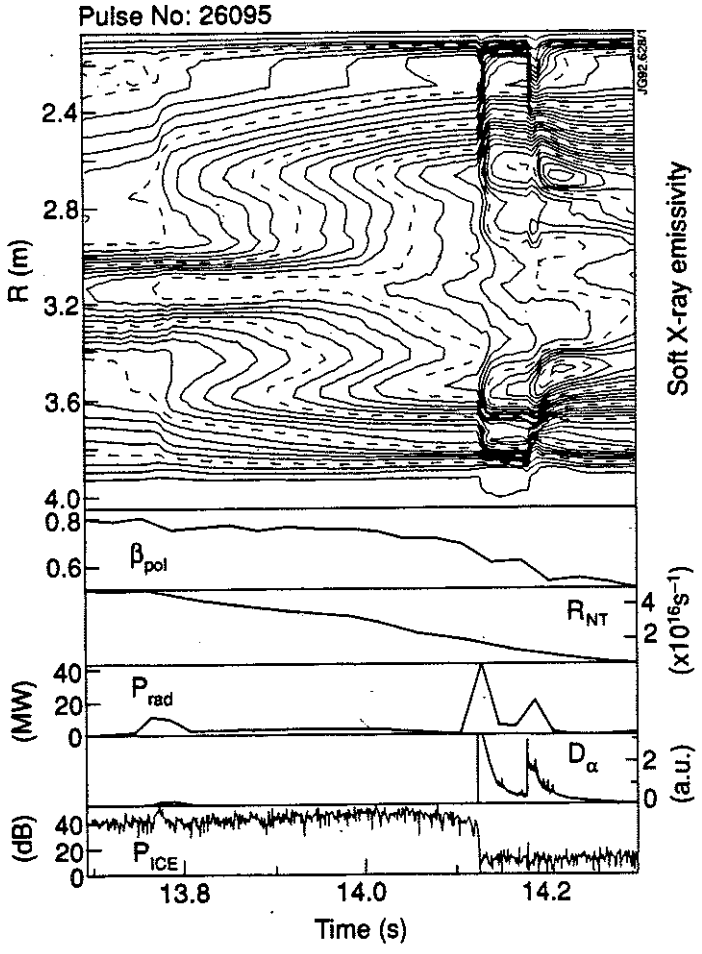

Fig 12: Evolution of the PTE pulse No. 26095 with 1 % tritium injection in two neutral beam sources. Above: reconstructed contours of soft X-ray emissivity as a function of time and major radius. Below: corresponding traces of β_{pol}, total neutron flux R_{NT}, total bolometric radiated power P_{rad}, a D_α signal, and the ICE intensity at fixed frequency $\nu = 33$ MHz.

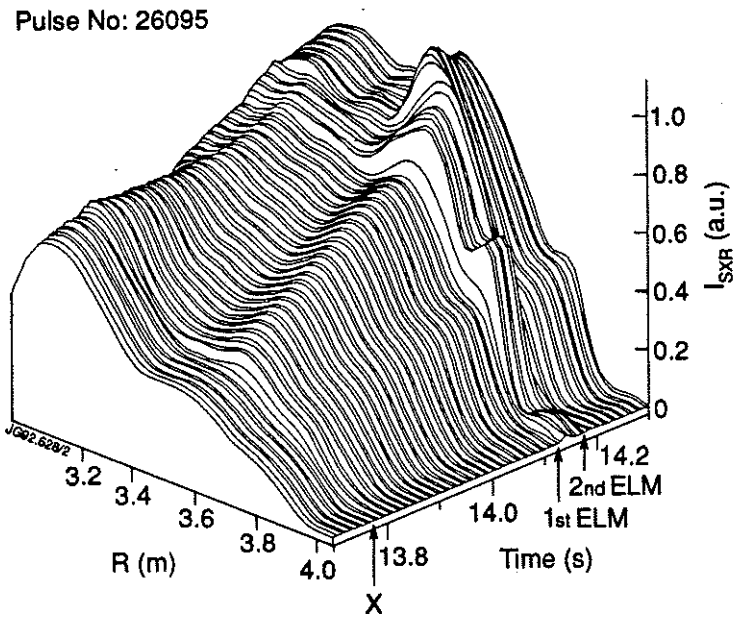

Fig 13: Isometric projection of the time-evolution of the reconstructed soft X-ray emissivity radial profile for pulse No. 26095. The time of the X-event is marked by symbol X, and the times of the two subsequent large amplitude ELMs are shown.

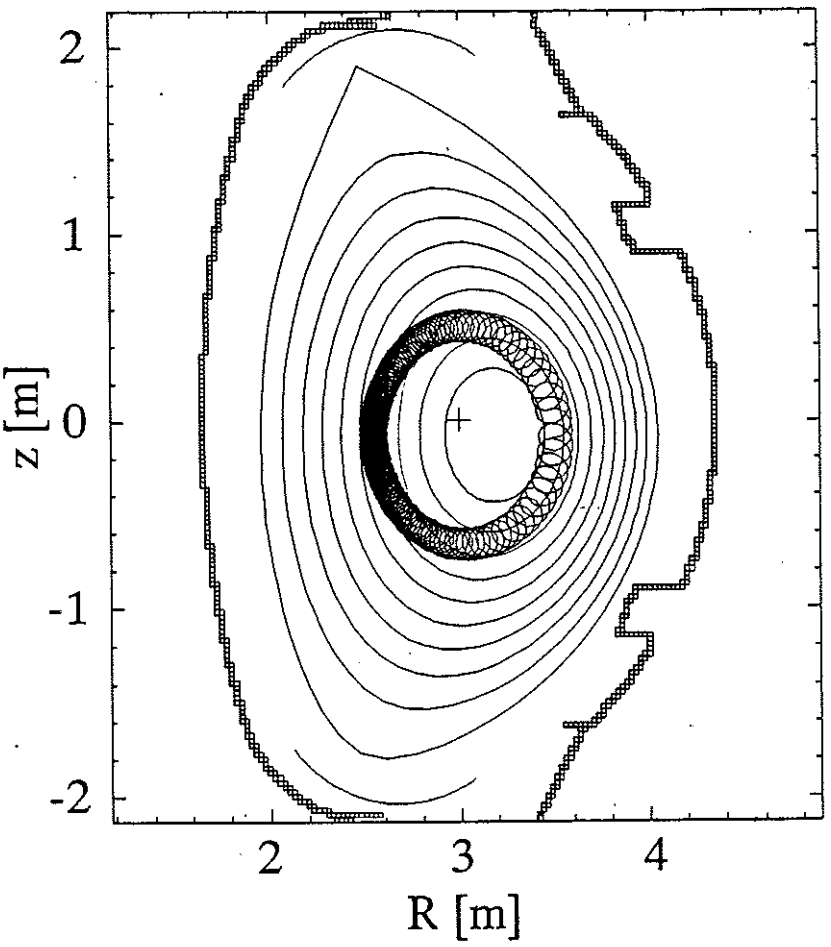
2
1
0
-1
-2
z [m]
2
3
4
R [m]

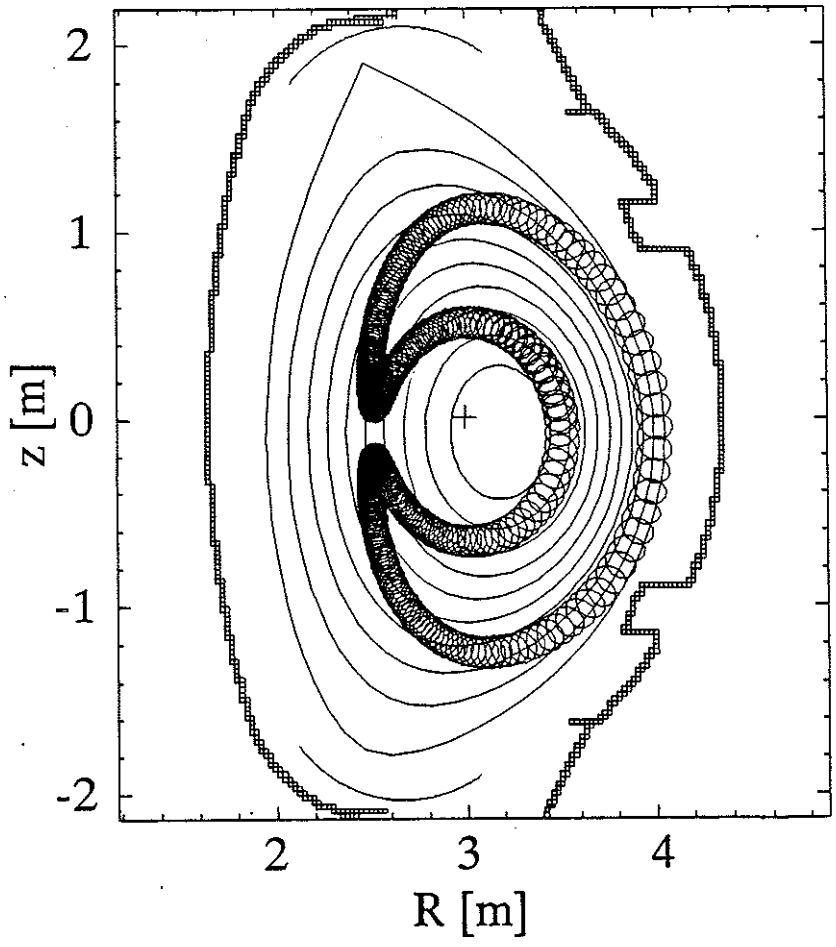
2
1
0
-1
-2
z [m]
2
3
4
R [m]

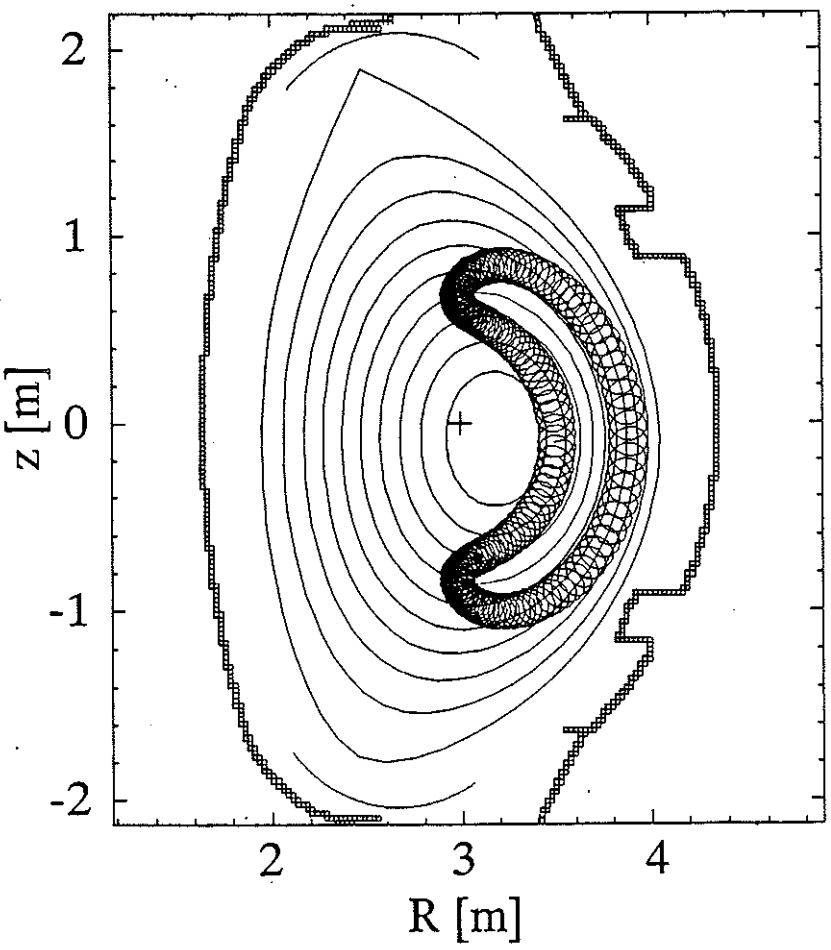

Fig 14: Poloidal projection of 3.5 MeV α-particle orbits in the flux-surface geometry of DT pulse No. 26148 at time 13.2 sec, close to the time of maximum neutron emission (see Fig. 6). In each case the particle was born at a point 33 cm from the magnetic axis in the mid-plane. (a) A passing orbit, just below the trapped-passing boundary - birth pitch-angle 54.8^{o}. (b) A large-excursion (LE) trapped orbit, just above the trapped-passing boundary - birth pitch-angle 55.2^{o}. (c) A trapped orbit which does not quite intercept $R = 4$ m - birth pitch-angle 65.1^{o}.

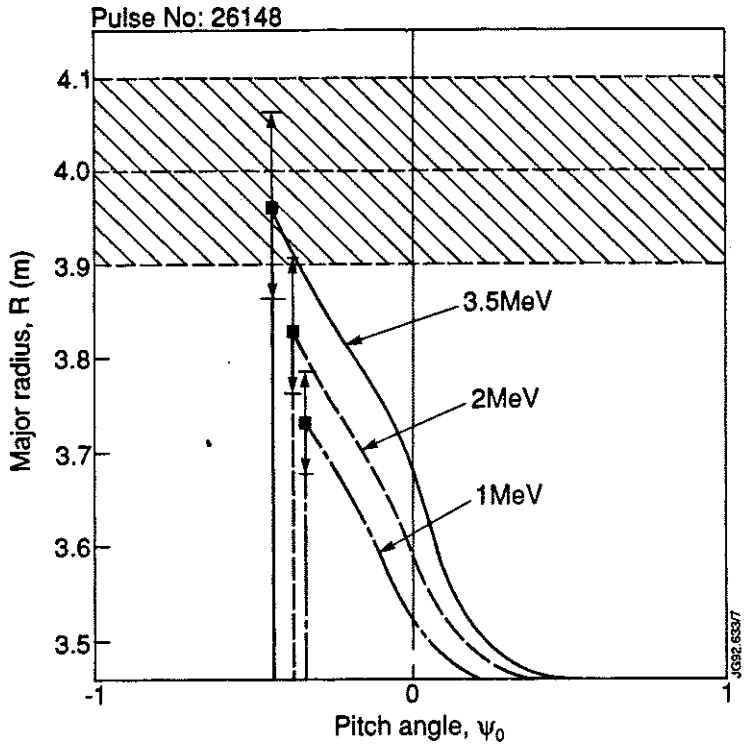

Fig 15: Plot of the maximum radial excursions of α-particle guiding-centre orbits as a function of the birth pitch-angle, for particle energies of 3.5 MeV, 2 MeV and 1 MeV. The hatched region (3.9 m ≤ R ≤ 4.1 m) represents the location of the ICE source. The vertical lines positioned at the maxima of each curve represent plus-or-minus one Larmor radius.

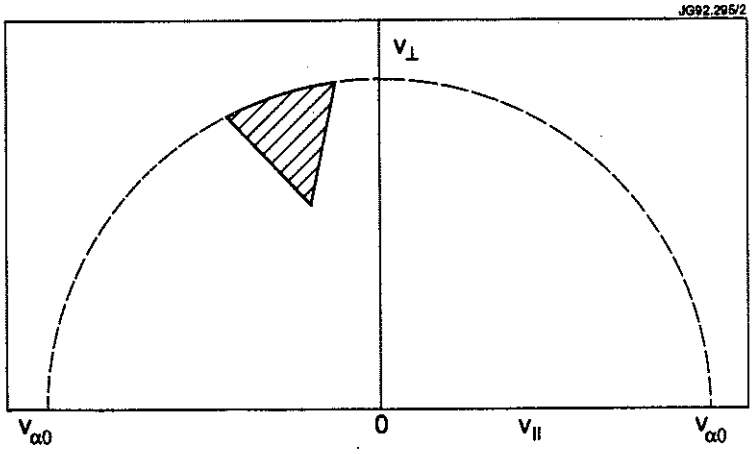

Fig 16: The region of velocity-space occupied by centrally born α-particles with large-excursion (LE) orbits at major radius R = 4.0 m. Parameters are for JET pulse No. 26148, as in Fig. 14.

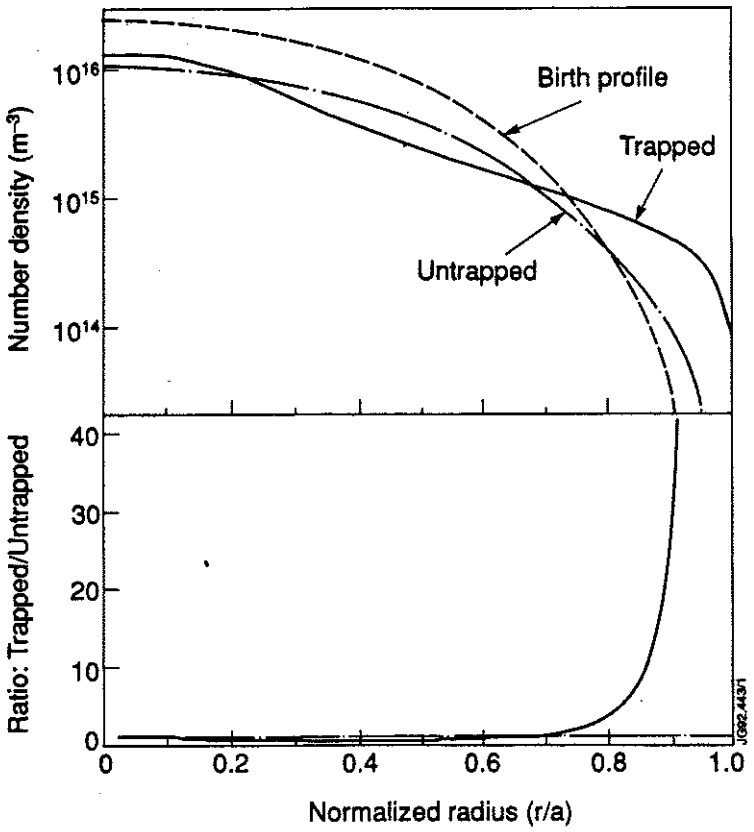

Fig 17: Above: profiles of the density of birth, trapped, and passing 3.5 MeV α-particles. Below: anisotropy ratio of trapped-to-passing α-particle density. The horizontal dashed line shows the isotropic case where the ratio of trapped-to-passing α-particle density equals unity.

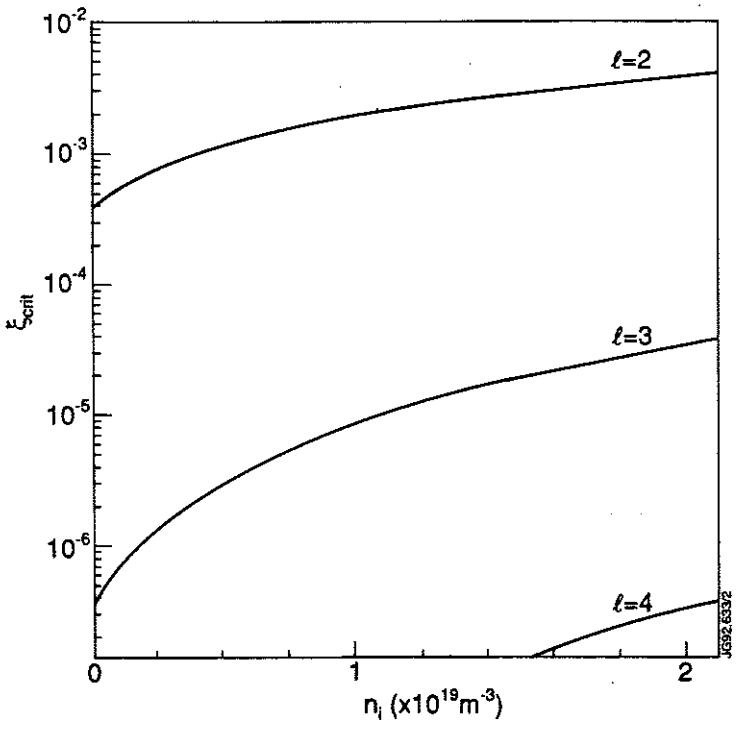

Fig 18: Plot of the critical α-particle concentration, ξ_{crit} , that is required to excite waves on the fast Alfven-cyclotron harmonic branch in the JET edge plasma, as a function of the thermal ion density.

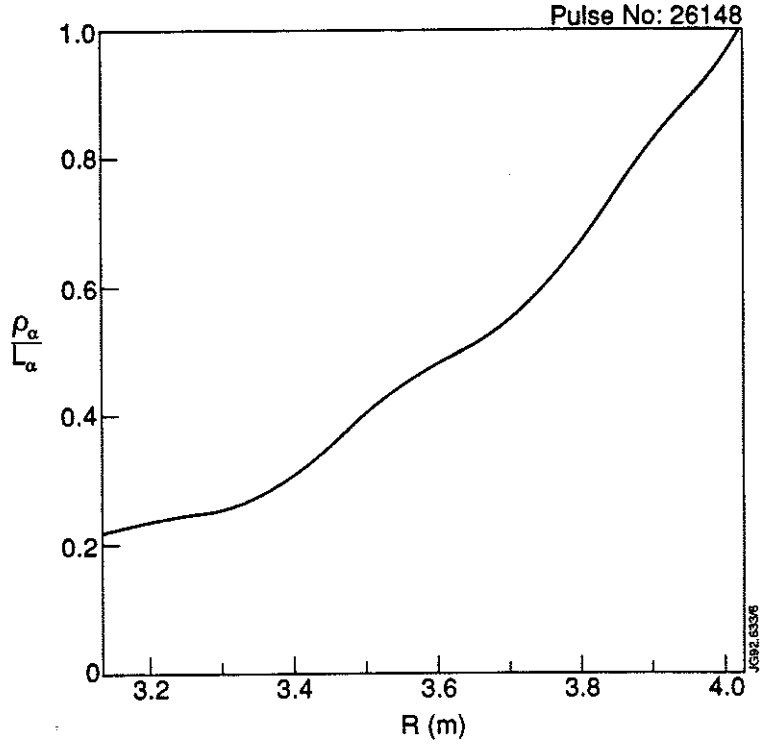

Fig 19: Radial profile of the ratio of the α-particle Larmor radius to the lengthscale of the radial α-particle density profile, based on TRANSP simulation of DT pulse No. 26148 at time $t = 13.2$ seconds.

Appendix I

THE JET TEAM

JET Joint Undertaking, Abingdon, Oxon, OX14 3EA, U.K.

J.M. Adams[1], B. Alper, H. Altmann, A. Andersen[14], P. Andrew, S.Ali-Arshad, W. Bailey, B. Balet, P. Barabaschi, Y. Baranov, P. Barker, R. Barnsley[2], M. Baronian, D.V. Bartlett, A.C. Bell, G. Benali, P. Bertoldi, E. Bertolini, V. Bhatnagar, A.J. Bickley, D. Bond, T. Bonicelli, S.J. Booth, G. Bosia, M. Botman, D. Boucher, P. Boucquey, M. Brandon, P. Breger, H. Brelen, W.J. Brewerton, H. Brinkschulte, T. Brown, M. Brusati, T. Budd, M. Bures, P. Burton, T. Businaro, P. Butcher, H. Buttgereit, C. Caldwell-Nichols, D.J. Campbell, D. Campling, P. Card, G. Celentano, C.D. Challis, A.V.Chankin[23], A. Cherubini, D. Chiron, J. Christiansen, P. Chuilon, R. Claesen, S. Clement, E. Clipsham, J.P. Coad, I.H. Coffey[24], A. Colton, M. Comiskey[4], S. Conroy, M. Cooke, S. Cooper, J.G. Cordey, W. Core, G. Corrigan, S. Corti, A.E. Costley, G. Cottrell, M. Cox[7], P. Crawley, O. Da Costa, N. Davies, S.J. Davies[7], H. de Blank, H. de Esch, L. de Kock, E. Deksnis, N. Deliyanakus, G.B. Denne-Hinnov, G. Deschamps, W.J. Dickson[19], K.J. Dietz, A. Dines, S.L. Dmitrenko, M. Dmitrieva[25], J. Dobbing, N. Dolgetta, S.E. Dorling, P.G. Doyle, D.F. Düchs, H. Duquenoy, A. Edwards, J. Ehrenberg, A. Ekedahl, T. Elevant[11], S.K. Erents[7], L.G. Eriksson, H. Fajemirokun[12], H. Falter, J. Freiling[15], C. Froger, P. Froissard, K. Fullard, M. Gadeberg, A. Galetsas, L. Galbiati, D. Gambier, M. Garribba, P. Gaze, R. Giannella, A. Gibson, R.D. Gill, A. Girard, A. Gondhalekar, D. Goodall[7], C. Gormezano, N.A. Gottardi, C. Gowers, B.J. Green, R. Haange, A. Haigh, C.J. Hancock, P.J. Harbour, N.C. Hawkes[7], N.P. Hawkes[1], P. Haynes[7], J.L. Hemmerich, T. Hender[7], J. Hoekzema, L. Horton, J. How, P.J. Howarth[5], M. Huart, T.P. Hughes[4], M. Huguet, F. Hurd, K. Ida[18], B. Ingram, M. Irving, J. Jacquinot, H. Jaeckel, J.F. Jaeger, G. Janeschitz, Z. Jankowicz[22], O.N. Jarvis, F. Jensen, E.M. Jones, L.P.D.F. Jones, T.T.C. Jones, J-F. Junger, F. Junique, A. Kaye, B.E. Keen, M. Keilhacker, W. Kerner, N.J. Kidd, R. Konig, A. Konstantellos, P. Kupschus, R. Lässer, J.R. Last, B. Laundy, L. Lauro-Taroni, K. Lawson[7], M. Lennholm, J.Lingertat[13], R.N. Litunovski, A. Loarte, R. Lobel, P. Lomas, M. Loughlin, C. Lowry, A.C. Maas[15], B. Macklin, C.F. Maggi[16], G. Magyar, V. Marchese, F. Marcus, J. Mart, D. Martin, E. Martin, R. Martin-Solis[8], P. Massmann, G. Matthews, H. McBryan, G. McCracken[7], P. Meriguet, P. Miele, S.F. Mills, P. Millward, E. Minardi[16], R. Mohanti[17], P.L. Mondino, A. Montvai[3], P. Morgan, H. Morsi, G. Murphy, F. Nave[27], S. Neudatchin[23], G. Newbert, M. Newman, P. Nielsen, P. Noll, W. Obert, D. O'Brien, J. O'Rourke, R. Ostrom, M. Ottaviani, S. Papastergiou, D. Pasini, B. Patel, A. Peacock, N. Peacock[7], R.J.M. Pearce, D. Pearson[12], J.F. Peng[26], R. Pepe de Silva, G. Perinic, C. Perry, M.A. Pick, J. Plancoulaine, J-P. Poffé, R. Pohlchen, F. Porcelli, L. Porte[19], R. Prentice, S. Puppin, S. Putvinskii[23], G. Radford[9], T. Raimondi, M.C. Ramos de Andrade, M. Rapisarda[29], P-H. Rebut, R. Reichle, S. Richards, E. Righi, F. Rimini, A. Rolfe, R.T. Ross, L. Rossi, R. Russ, H.C. Sack, G. Sadler, G. Saibene, J.L. Salanave, G. Sanazzaro, A. Santagiustina, R. Sartori, C. Sborchia, P. Schild, M. Schmid, G. Schmidt[6], H. Schroepf, B. Schunke, S.M. Scott, A. Sibley, R. Simonini, A.C.C. Sips, P. Smeulders, R. Smith, M. Stamp, P. Stangeby[20], D.F. Start, C.A. Steed, D. Stork, P.E. Stott, P. Stubberfield, D. Summers, H. Summers[19], L. Svensson, J.A. Tagle[21], A. Tanga, A. Taroni, C. Terella, A. Tesini, P.R. Thomas, E. Thompson, K. Thomsen, P. Trevalion, B. Tubbing, F. Tibone, H. van der Beken, G. Vlases, M. von Hellermann, T. Wade, C. Walker, D. Ward, M.L. Watkins, M.J. Watson, S. Weber[10], J. Wesson, T.J. Wijnands, J. Wilks, D. Wilson, T. Winkel, R. Wolf, D. Wong, C. Woodward, M. Wykes, I.D. Young, L. Zannelli, A. Zolfaghari[28], G. Zullo, W. Zwingmann.

PERMANENT ADDRESSES

1. UKAEA, Harwell, Didcot, Oxon, UK.
2. University of Leicester, Leicester, UK.
3. Central Research Institute for Physics, Budapest, Hungary.
4. University of Essex, Colchester, UK.
5. University of Birmingham, Birmingham, UK.
6. Princeton Plasma Physics Laboratory, New Jersey, USA.
7. UKAEA Culham Laboratory, Abingdon, Oxon, UK.
8. Universidad Complutense de Madrid, Spain.
9. Institute of Mathematics, University of Oxford, UK.
10. Freien Universität, Berlin, F.R.G.
11. Royal Institute of Technology, Stockholm, Sweden.
12. Imperial College, University of London, UK.
13. Max Planck Institut für Plasmaphysik, Garching, FRG.
14. Risø National Laboratory, Denmark.
15. FOM Instituut voor Plasmafysica, Nieuwegein, The Netherlands.
16. Dipartimento di Fisica, University of Milan, Milano, Italy.
17. North Carolina State University, Raleigh, NC, USA
18. National Institute for Fusion Science, Nagoya, Japan.
19. University of Strathclyde, 107 Rottenrow, Glasgow, UK.
20. Institute for Aerospace Studies, University of Toronto, Ontario, Canada.
21. CIEMAT, Madrid, Spain.
22. Institute for Nuclear Studies, Otwock-Swierk, Poland.
23. Kurchatov Institute of Atomic Energy, Moscow, USSR
24. Queens University, Belfast, UK.
25. Keldysh Institute of Applied Mathematics, Moscow, USSR.
26. Institute of Plasma Physics, Academica Sinica, Hefei, P. R. China.
27. LNETI, Savacem, Portugal.
28. Plasma Fusion Center, M.I.T., Boston, USA.
29. ENEA, Frascati, Italy.

At 1st July, 1992